

## High-Frequency Variability Induced in the Southern California Bight by a Wind Event in Sebastián Vizcaíno Bay, Baja California



### Key Points:

- After a short wind burst, Sebastián Vizcaíno Bay is a continuous source of surface gravity waves, internal waves, and coastal-trapped waves
- Variability associated with Sebastián Vizcaíno Bay occurs at its natural resonance frequency of 5.2 cpd
- Sebastián Vizcaíno Bay enhances vertical velocity variance throughout the Southern California Bight and SSH variability along the coast

### Supporting Information:

Supporting Information may be found in the online version of this article.

### Correspondence to:





K. Ramos-Musalem,  
[kramosmu@atmosfera.unam.mx](mailto:kramosmu@atmosfera.unam.mx)

### Citation:

Ramos-Musalem, K., Gille, S. T., Cornuelle, B. D., & Mazloff, M. R. (2023). High-frequency variability induced in the Southern California Bight by a wind event in Sebastián Vizcaíno Bay, Baja California. *Journal of Geophysical Research: Oceans*, 128, e2022JC019547. <https://doi.org/10.1029/2022JC019547>

Received 5 DEC 2022

Accepted 9 MAY 2023

K. Ramos-Musalem<sup>1</sup> , S. T. Gille<sup>2</sup> , B. D. Cornuelle<sup>2</sup> , and M. R. Mazloff<sup>2</sup> 

<sup>1</sup>Instituto de Ciencias de la Atmósfera y Cambio Climático, Universidad Nacional Autónoma de México, Ciudad de México, México, <sup>2</sup>Scripps Institution of Oceanography, University of California, San Diego, La Jolla, CA, USA

**Abstract** Although the California Current System extends as far south as the southern tip of the Baja California Peninsula (BCP), some past model domains have employed an open boundary near the Mexico-US border, excluding Sebastián Vizcaíno Bay (SVB), a hook-like coastal feature at mid-length of the BCP. An earlier modeling study has shown the SVB to be a previously unknown forcing region that governs SSH variability in the Southern California Bight (SCB). Motivated by that evidence, our aim is to understand the variability that originates from the SVB and to identify what is lost in a numerical model of the SCB when the SVB is excluded. To do this we use an idealized configuration of the MITgcm, without tides, using the bathymetry with the bay and comparing it to model runs where the bay is removed. Our results show that a short wind event ( $\leq 4$  hr) blowing over SVB can enhance variability everywhere in the domain. First, the event excites a seiche in the bay at frequency 5.2 cpd. Then, seiche energy leaks into the domain in the form of gravity waves that are topographically amplified in the SCB, coastal trapped waves (CTWs) that travel north along the coast, and internal waves, that enhance vertical velocity variance at particular depths by up to 27% compared to experiments without the SVB. Given the frequency of wind events like the one modeled, our results suggest that the SVB is a continuous source of gravity waves, internal waves, and CTWs to the SCB.

**Plain Language Summary** Sebastián Vizcaíno Bay (SVB) is a huge hook-like coastal feature midway along the Baja California Peninsula, Mexico. Previous studies have found evidence that the wind blowing over the SVB generates waves that influence sea surface height (SSH) variability at the Southern California Bight (SCB), off the Southern California Coast. This study identifies the wind-generated waves produced at the SVB and asks how they travel across the ocean in the region off northern Baja California and the SCB. We use a simplified ocean computer model that spans the SVB and the SCB, forced only by a short wind burst over the ocean. We isolate the waves generated by the SVB by comparing the model results to an identical model from which we have artificially removed the SVB. The wind blowing over the bay forces an oscillation within the bay and also generates waves (at the surface and in the ocean interior) that propagate away from the bay. Accounting for these oscillations in models of the SCB is important for predicting processes such as changes in SSH along the coast and mixing of deeper, nutrient-rich water up to biologically relevant depths of the ocean.

## 1. Introduction

Regional numerical models have open ocean boundaries with conditions that need to be specified to ensure that the model reproduces the physics of the ocean. These conditions limit the variability that can be reproduced in the model (Dong et al., 2009; Kerry et al., 2013; Mazloff et al., 2020; Nelson et al., 2020). In particular, models can omit variability due to the dynamical effect of topographic features outside the domain.

The California Current System (CCS) has been extensively modeled with different aims and numerical configurations (e.g., Dong et al., 2009; Mazloff et al., 2020; Molemaker et al., 2015; Moore et al., 2011; Neveu et al., 2016; Todd et al., 2011). Although the CCS extends as far south as the southern tip of the Baja California Peninsula (Hickey, 1998), many study domains have a southern boundary near the Mexico-US border. This excludes the Sebastián Vizcaíno Bay (SVB), a huge hook-like feature at mid-length of the Baja California Peninsula (Figure 1a), which has the potential to be an important source of sea surface height (SSH) variability in the Southern California Bight (SCB)—the region off the Southern California coast that is roughly bounded by San Diego to the south, Point Conception to the north and the Santa Rosa Ridge to the west (Figure 1a). Our aim is

© 2023 The Authors.

This is an open access article under the terms of the [Creative Commons Attribution-NonCommercial License](https://creativecommons.org/licenses/by-nc/4.0/), which permits use, distribution and reproduction in any medium, provided the original work is properly cited and is not used for commercial purposes.

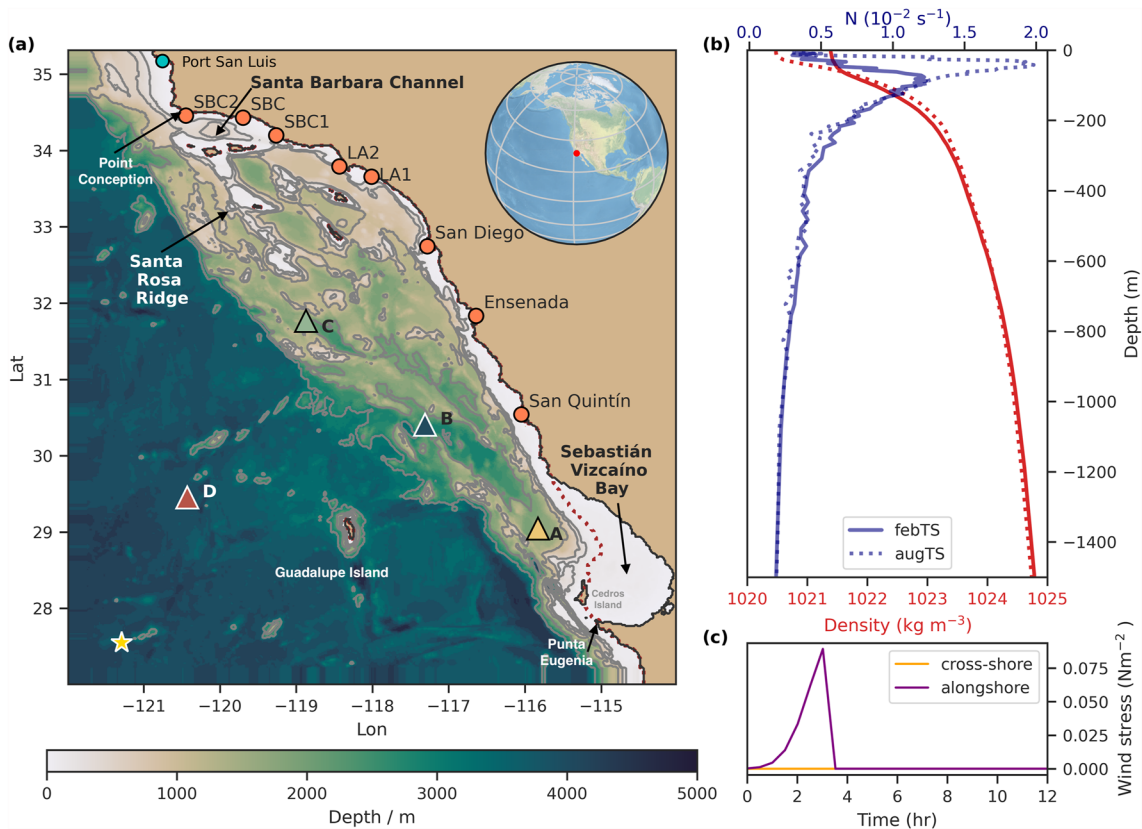


**Figure 1.** (a) Model domain and bathymetry where the gray contours correspond to the 250, 500, 1,000, 2,000 and 3,000 m isobaths; the brown, dotted contour corresponds to the coastline in the experiments without Sebastián Vizcaíno Bay (SVB), orange markers indicate key virtual stations used as reference points along the coast, and the yellow, star corresponds to the location where initial temperature and salinity profiles were taken from the CASE-STSE model. (b) Density and buoyancy frequency profiles in the top 1,500 m of the numerical experiments with winter (FebTS) and summer (AugTS) temperature and salinity conditions. (c) Alongshore wind stress forcing peaked at 3.5 hr and then dropped to zero for the rest of the 5-day simulation.

to understand the variability that originates from the SVB and to identify what is lost when the SVB is excluded from numerical models.

Evidence of the importance of the SVB was reported by Verdy et al. (2014), who used an adjoint model to find the sensitivity of SSH to wind stress at Port San Luis, located on the coast of California at 35.16°N. The model disclosed an unsuspected remote forcing region in the SVB. Maps of SSH sensitivity to along- and cross-shore wind stress (Figure 6 in Verdy et al., 2014) show that SSH at Port San Luis has a fast response to local wind stress, as expected, but also, that remote winds in the SVB generate a response 1–12 hr after the wind blows over the bay. Verdy et al. (2014) hypothesized that a resonance mechanism in the bay generates and sustains fast-traveling coastal waves.

The SCB has a complex coastline and topography, interrupted by numerous islands and ridges. The circulation in the SCB and along the Pacific Coast of Northern Baja California is influenced by the California Current and undercurrent (e.g., Hickey, 1979), local atmospheric forcing (Hickey, 1979; Lynn & Simpson, 1987), and tropical and equatorial remote forcing through the coastal wave guide (e.g., Christensen et al., 1983; Gómez-Valdivia et al., 2017). Moreover, the coast off Baja California, approximately from 25° to 31°N, is known to correspond to a transition zone for the CCS (Durazo, 2015; Durazo & Baumgartner, 2002; Hickey, 1979; Lynn & Simpson, 1987).

This paper builds on the work of Verdy et al. (2014) to characterize the impact that the SVB has on SSH and vertical velocity variability in the SCB after a short, yet intense, wind event. We run an idealized configuration of the Massachusetts Institute of Technology general circulation model (MITgcm) using the full bathymetry of the bay and compare it to a model run with the bay removed from the bathymetry. The results show the impact of a wind event over the SVB on the regional circulation.

As we will show, the effect of the bay is to increase variability in the domain. This happens through several mechanisms. First, wind forcing excites a seiche in the SVB. Then, energy from the seiche leaks into the domain in the form of long, barotropic gravity waves, coastal-trapped waves (CTWs), and internal waves (IWs). Besides the variability generated directly due to energy leaking from the bay, the gravity waves drive other sources of variability in the domain by exciting IWs as they propagate over complex topography in the SCB, amplifying the natural oscillations of the smaller bays along the coast, and being topographically amplified at the SCB, especially in the Santa Barbara Channel (SBC).

This paper is organized as follows: In Section 2 we describe the model configuration and numerical experiments. In Section 3 we present results. In Section 3.3 we report on the wind-driven SSH response in the bay, in Sections 3.4–3.6 we explain the impact of the bay on SSH within the domain and along the coast, and in Section 3.7 we describe the effect of the bay on vertical velocity within the domain. Finally, in Section 4 we discuss our findings.

## 2. Methods

### 2.1. Model Configuration

We use the MITgcm (Marshall et al., 1997) to simulate an upwelling-favorable wind event (wind burst) blowing uniformly over the Pacific coast of Northern Baja California and the SCB (Figure 1a). The model domain extends from 27° to 35.3°N and from 122° to 114°W. It is discretized into 512 × 612 horizontal grid cells for a resolution of 1.5 km ± 10% (or  $\Delta x = 0.016^\circ$ ,  $\Delta y = 0.014^\circ$ ). In the vertical, 100 z-levels are distributed over a total depth of 4,700 m, with a resolution that smoothly transitions from 2 m at the surface to 270 m at 4,700 m depth, with adjacent vertical separations differing by no more than 10%. The varying depth spacing was adjusted to resolve the stratification with maximum potential density increments of 0.08–0.15 kg m<sup>-3</sup> happening where the level spacing is 2 m (Figure S1 in Supporting Information S1).

The model uses realistic bathymetry from GEBCO (2020), slightly smoothed for better performance. The smoothing procedure follows the smoothing functions provided in ROMSTOOLS (Penven et al., 2008), translated to Python and adapted for our domain, and consists of a selective filter applied to reduce isolated seamounts in the deep ocean, followed by a single pass of a Hanning filter to ensure that there is no 2D noise in the topography. In preliminary experiments, we noticed that the smoothness of the bathymetry can modify the vertical structure of the IWs, but this effect will be studied in detail in future work. Additionally, we flatten the topography at the 15 grid cells adjacent to the open boundaries so that there are no topography gradients across the open boundaries.

The simulation starts from rest and is forced by an approximately along-shore wind stress that evolves following the first half of the Gaussian function

$$\tau_{\parallel} = [1 - H(t - t_c)]\tau_{\max} e^{-\frac{(t-t_c)^2}{2\sigma}} \quad (1)$$

where  $t > 0$  is time,  $H(t)$  is the Heaviside step function,  $t_c = 3.5$  hr is the time when the forcing reaches the maximum value of  $\tau_{\max} = 0.1$  Pa, and  $\sigma = 1$ . The forcing stops after the maximum magnitude has been reached. In theory, we would prefer to have an abrupt forcing function, such as a delta or step function to excite the system with every possible frequency. Instead, we chose the Heaviside forcing in (Equation 1) that has enough power to excite the frequencies we are interested in and a smoother shape that only filters the higher frequencies that would already be damped due to the temporal and spatial resolution of the model. Additionally, we tested longer (4.5 hr) and shorter (2.5 hr) wind pulses and found that the relevant frequencies excited in the domain remained the same. In total, the model is run for 5 days, forced only for the first 3.5 hr, and does not include tides. The direction of the wind stress is at  $-33^\circ$  with respect to east, blowing toward the southeast, approximately parallel to the coast of Baja California (as in Verdy et al., 2014; Figure 1).

The domain has open boundaries at the north, south, and west with Orlandi radiation conditions (Orlandi, 1976). These open boundary conditions may seem like an odd choice given the results of for example, Palma and Matano (1998) and Siyanbola et al. (2023); however, we see no reflections of internal or surface gravity waves at the boundaries, and the results are robust to changes in the size of the domain. At the bottom and sides boundary conditions are free-slip. In preliminary runs, we noticed that no-slip conditions at the bottom make no difference in

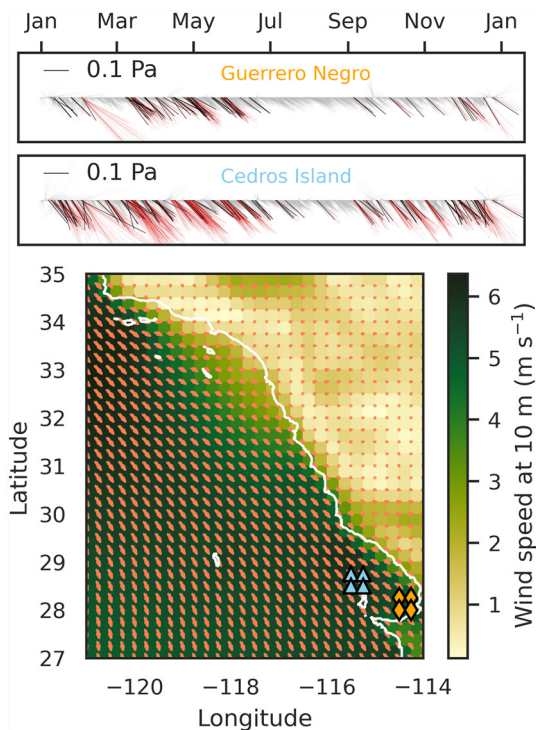


**Figure 2.** Hourly wind speed and velocity at 10 m averaged over 1 year (2016) taken from the ERA5 data set (Hersbach et al., 2018) show that winds are predominantly toward the southeast in the domain, particularly over SVB (panel c). Hourly wind stress vectors at two locations, close to Cedros Island and Guerrero Negro (averages over triangles and diamonds in panel c, respectively), in SVB show that wind stress is predominantly toward the southeast in the bay (gray sticks). Red sticks show the times in which wind stress magnitude is greater than 0.1 Pa and directions are between  $-25^\circ$  and  $-90^\circ$  degrees with respect to east, and black sticks correspond to the beginning of each event with the characteristics described before. We identify 76 events at Guerrero Negro and 119 events at Cedros Island throughout 2016.

29.8°N, taken from the 150 m isobath to the coast, was extended south following the same 150 m isobath up to Punta Eugenia, in the southern tip of SVB. The resulting coastline is shown in Figure 1a with a brown, dotted line. The strategy adopted here follows an approach used in a number of recent studies that have removed topographic features from the bathymetry to characterize and quantify their impact on the circulation and dynamics of the flow (e.g., Connolly & Hickey, 2014; Gopalakrishnan & Cornuelle, 2019; Li et al., 2021; Saldías et al., 2021).

In this idealized scenario, the model results are consistent with the physical behavior we expect to find. In particular, we are interested in identifying signals generated at SCB that may arrive at Port San Luis between 1 and 12 hr after they are excited (See, Verdy et al., 2014; Figure 6). Port San Luis is about 950 km away from SVB, which means we are looking for signals that travel between 79 and 950 km hr<sup>-1</sup> or between 22 and 264 m s<sup>-1</sup>. Indeed, we find signals traveling at a variety of speeds, including gravity waves moving at approximately 500 km hr<sup>-1</sup>. There are even faster signals that appear as disturbances to sea surface height before the wind forcing stops. This is not surprising given that there are regions in the domain where the maximum depth is between 3,000 and 4,000 m, which means that barotropic signals can propagate as fast as 713 km s<sup>-1</sup> (199 m s<sup>-1</sup>).

### 2.3. Are Wind-Burst Events Common in SVB?

Winds over the SVB are predominantly toward the southeast all year long (Figure 2c) and drive a region of sustained, year-round, wind-driven upwelling (e.g., Kämpf & Chapman, 2016). Relaxation events, required here as much as the upwelling winds themselves, are also common in the region (Vazquez & Gomez-Valdes, 2021).

the evolution of the surface seiche in the bay or in the IW structure, however, in runs with a combination of bottom friction and bottom drag we found that the amplitude of the seiche in the bay can decrease by as much as 50% in the stratified run, but the effect is linear. So, the mechanism that we describe for seiche dissipation throughout the results is not changed by having bottom friction, but the magnitudes of SSH, vertical velocity and displacement, and derived quantities would be proportionally smaller. In short, adding bottom friction does not affect the mechanism of seiche dissipation described here, but it does reduce the absolute magnitudes reported.

The time step used was 60 s for the stratified runs and 30 s for the barotropic runs, while output was saved every 10 min for the 5 days of simulation. We use a linear equation of state, with thermal expansion and haline contraction coefficients  $\alpha_T = 2.0 \times 10^{-4} \text{ }^\circ\text{C}^{-1}$  and  $\beta_S = 7.4 \times 10^{-4}$ , respectively.

Momentum and tracer dissipation in the interior are characterized by horizontal viscosity and diffusivity coefficients  $A_h = K_h = 100 \text{ m s}^{-2}$  and vertical viscosity and diffusivity coefficients  $A_z = K_z = 10^{-5} \text{ m s}^{-2}$ , respectively. Additional numerical diffusivity is introduced to the solution by the advection scheme, which is a linear, second-order centered scheme.

### 2.2. Numerical Experiments

In this study, we analyze three runs with different density distributions: one with no stratification (barotropic), and two with horizontally homogeneous stratification representative of winter and summer conditions offshore in the domain (Figure 1b). In these cases, initial, vertical temperature and salinity profiles are the same everywhere, corresponding to February (FebTS) and August (AugTS) 2008 monthly mean fields calculated at (121.3°W, 27.6°N) in the California State Estimate (CASE-STSE) model output (yellow triangle in Figure 1a). FebTS will serve as the base case in the results section. There are no tides in the experiments.

For all three runs, we repeated the same integration with identical dynamical conditions, except that the bathymetry did not include the SVB (hereafter referred to as noSVB cases). To remove the bay, the cross-shelf slope at



As an example of the recurrence of upwelling-favorable wind events, we look at a year of hourly reanalysis wind data from ERA5 at the SVB (2016), downloaded from the Copernicus Climate Change Service (C3S) Climate Data Store (Hersbach et al., 2018). We convert 10-m wind speeds into wind stress components, using the drag coefficient parametrization proposed by Large and Pond (1981). The stick plots in Figures 2a and 2b show the direction and magnitude of hourly wind stress, colored red whenever the wind stress direction is southeast, meaning between  $-25^\circ$  and  $-90^\circ$  with respect to east (southeast direction), and magnitude equal or higher than 0.1 Pa, which is the maximum forcing applied in our model, at two locations within SVB. Applying these restrictions, we identify 76 events close to the coast (Guerrero Negro) and 119 wind events close to the mouth of SVB (Isla Cedros) with a duration between 1 and 64 hr. We consider that the number of wind events found in this particular year supports the effort of studying the response of the bay to wind bursts like the one modeled here.

### 3. Results

#### 3.1. Response of the Domain to a Wind Event in SVB

In all runs, as the wind forcing increases, water piles up in the southeastern end of the domain, generating an increase in SSH; while SSH decreases on the opposite side, as a consequence of the winds blowing toward the southeast ( $-30^\circ$  with respect to E). The magnitude of this forced SSH variation is determined everywhere by the shape of the coastline and the topography (Movie S1, left column). The water pile-up is largest in the southeast boundary of the SVB, with a maximum SSH  $\geq 1$  cm as wind stress reaches its maximum value of 0.1 Pa, while sea level dips most strongly at the coast near Santa Barbara and Long Beach ( $\geq 5$  mm), at the northern boundary of SVB ( $\sim 4$  mm), and within the islands in the SCB (2.5–4 mm) (Movie S1 at 3.5 hr, bottom left panel). Along the coast, wind forcing causes SSH to dip along the northern edge of the many bays and bends of the coastline, except at Todos Santos Bay, Ensenada, where there is a positive perturbation to SSH (Movie S1 at 3.5 hr, top left panel).

When the wind forcing stops after 3.5 hr, all the positive and negative SSH perturbations evolve freely, including oscillations. These oscillations appear to have the largest amplitudes where the initial SSH perturbations were strongest (i.e., SVB, SCB, and smaller bays along the coast). There is a small ( $\leq 1$  mm) domain-wide, SSH oscillation.

All oscillations decay in time, and by the end of the first day, only oscillations at the SVB can be clearly seen in the Movie S1. After 10 hr, a general decrease in SSH along the coast between the SVB and Santa Monica starts setting up as a consequence of the waveguide starting the process of geostrophic adjustment (Movie S1, left panels).

Along the coast, SSH varies on several time scales. A Hovmöller diagram of SSH at all model grid points along the coast shows that, as the wind intensifies, water piles up or dips at the smaller bays along the coast, and when the wind forcing stops, they oscillate at their natural frequencies, particularly during the first day of simulation (e.g., San Quintin, Bahía Todos Santos (Ensenada), and San Diego in Figure 3b). The frequency spectra of SSH show that these oscillations are composed of several frequencies, and the dominant frequencies vary for each bay (Figure S2a in Supporting Information S1). Lower frequency oscillations with periods on the order of a day can also be seen in Figure 3a.

#### 3.2. Energy Partition

The wind blows over the domain for 3.5 hr. The total wind energy input over the whole domain in the run with the bay (SVB) integrated over the forcing time is  $1.72 \times 10^{13}$  J, while the run without the bay (noSVB) receives  $1.67 \times 10^{13}$  J. The energy input into the SVB alone is  $4.93 \times 10^{11}$  J. This means that the area of the bay, which is 3% of the total area of the domain, allows 3% more wind energy input into the SVB run, than in the noSVB run (See Appendix A for energy estimates).

In both simulations, kinetic energy (KE) in the domain evolves following the wind energy input (Figure 4a) and reaches a maximum value of  $1.54 \times 10^{13}$  J in the SVB run and  $1.49 \times 10^{13}$  J in the noSVB run after 3.5 hr, which account for approximately 90% of the total wind energy input in each case. However, the maximum KE is 3.4% larger in the SVB run compared to the noSVB run, which is 13% larger than the initial wind energy input difference. After the forcing stops, KE decreases throughout the simulation due to dissipation.

As described previously, on timescales of hours to a few days, the main response to a wind-forcing event appears in SSH. The potential energy (SPE) associated with changes in SSH ( $O(10^9)$  J) is much smaller than KE in the

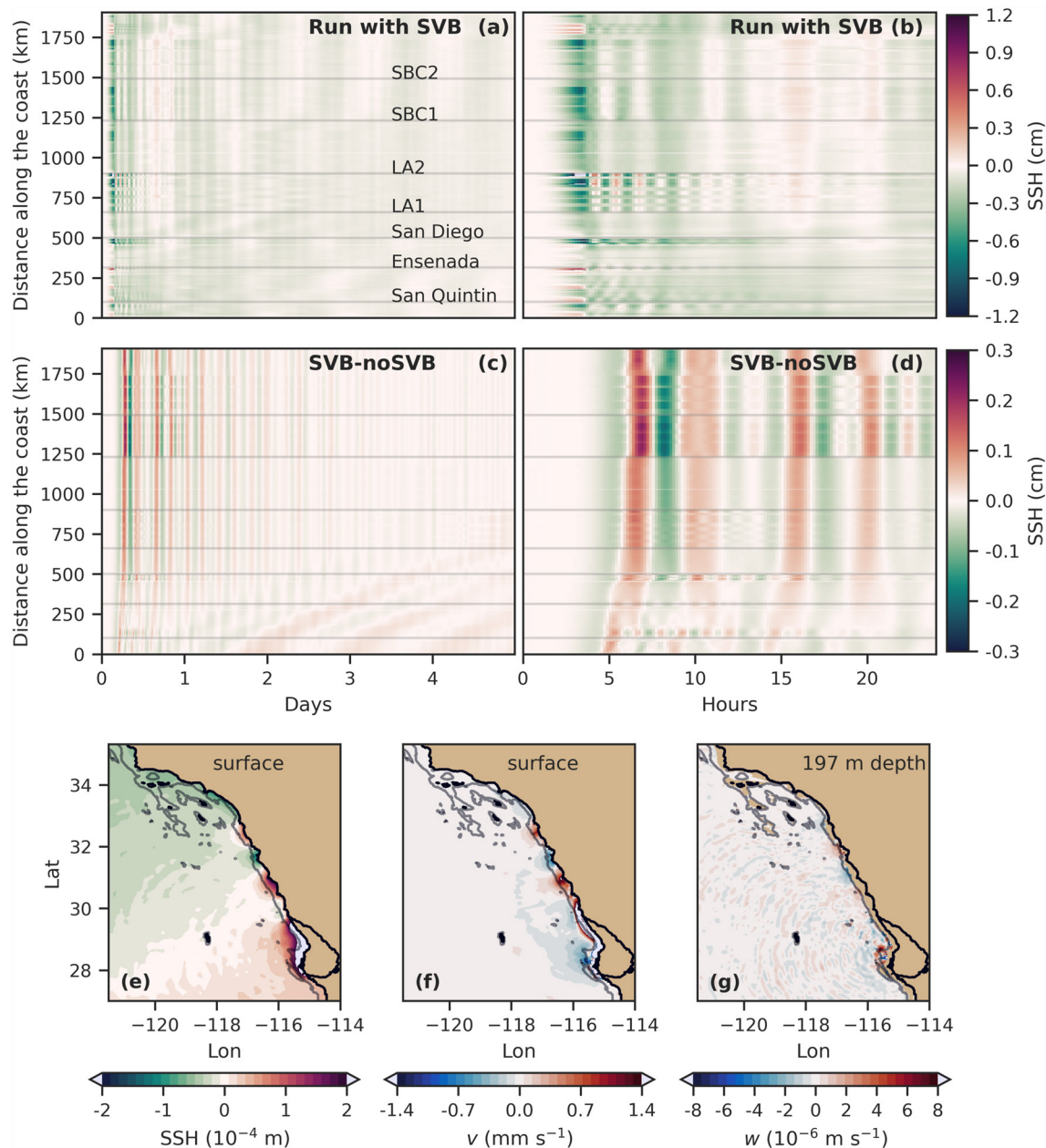


**Figure 3.** Sea surface height (SSH) along the coast starting outside the northern limit of Sebastián Vizcaíno Bay for the run with bay (a) and the difference between experiments with bay and without the bay (c) during the whole simulation and close up during the first day (b and d). Note the ringing of bays along the coast in (b). There are two types of surface signals generated by the bay propagating through the domain and up the coast: fast barotropic waves (positive and negative stripe pattern in c and d) that are amplified as they travel north and particularly so around Santa Barbara Channel, and slower, baroclinic signals (tilted, positive stripes in c). We identify these signals in snapshots of SVB-induced (e) SSH, (f) meridional velocity at surface and (g) vertical velocity at 197 m taken after 3.5 days of simulation as a northward propagating CTW that has traveled from Sebastian Vizcaino Bay to the Southern California Bight. The gray contour corresponds to the 500 m depth isobath.

domain ( $O(10^{13})$  J); however, sPE in the SVB run is 4 times larger than in the noSVB run during the first day of simulation (Figure 4b) and oscillates in time after the forcing stops.

Stratification in the system reduces the KE and sPE, allowing an alternative pathway for wind energy, which is not through the KE or sPE calculated here. This dissipation occurs through the radiation of internal waves from the bay (Cerovečki et al., 1997; Cushman-Roisin et al., 2005; Parsmar & Stigebrandt, 1997), a mechanism that will be further discussed in Section 3.3. The barotropic runs with and without the bay show larger KE and sPE compared to the stratified runs (FebTS). The difference in KE shows a peak that follows the forcing, and the

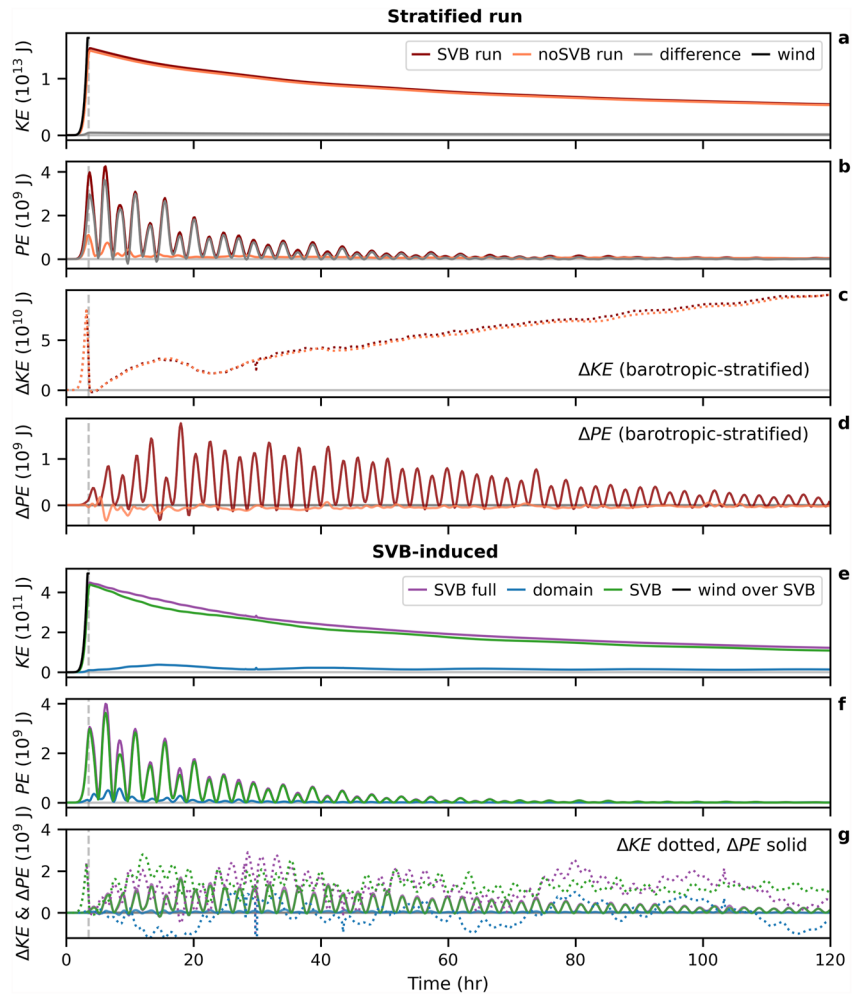


**Figure 4.** (a) Kinetic energy and (b) potential energy associated with changes in SSH in the whole domain for the stratified base run FebTS with (SVB run) and without (noSVB run) the SVB. Energy differences with respect to the corresponding barotropic runs show that the barotropic case has larger KE (c) and sPE (d) when the bay is present, and larger KE and lower sPE when there is no SVB. The total SVB-induced changes in KE (e) and sPE (f) (purple lines) in the whole domain are dominated by local changes within the bay (green lines). The effect of the bay in the rest of the domain is represented by the blue lines (e–g). (g) The difference between barotropic and baroclinic contributions to KE and sPE induced by the SVB shows that on average more KE moves from the bay to the domain when there is stratification (blue dotted line).

difference increases in time after the first day ( $\Delta KE O(10^{10})$ ) (Figure 4c). Potential energy is always larger in the barotropic run with the bay, and the difference in sPE oscillates in time; however, sPE is larger in the baroclinic run without the bay, and the difference between barotropic and baroclinic runs is much smaller ( $\sim 10\times$ ) than in the SVB run (Figure 4d). This is because the seiche in the bay, which is driving the largest change in SSH, and thus in sPE, is not present in the noSVB run. Moreover, sPE is larger in the barotropic case because the seiche is less attenuated, as will be shown later.

### 3.2.1. The Effect of the SVB

The excess wind energy input due to the bay is 3% of the total wind forcing. Maximum KE due to the velocities induced by the bay, calculated as the difference between the velocities in the SVB run and noSVB run account for 90% of the excess wind forcing energy input (Figure 4e). Of all the KE induced by SVB, KE in the bay accounts for 100% and this contribution decreases to 85% by day 5. On the other hand, KE in the rest of the domain is 0% at the beginning of the simulation and increases to 15% by day 5. This shows that the SVB provides KE to the domain (Figure 4e). In the absence of stratification, the SVB contribution to KE is larger than in the stratified

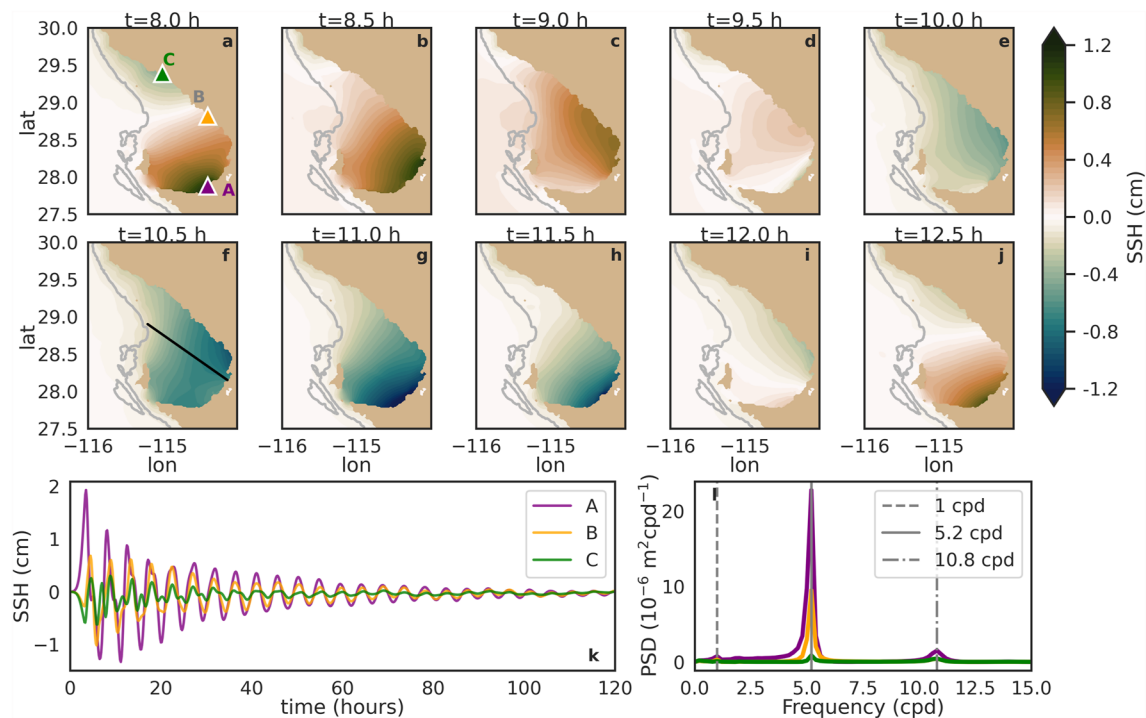


**Figure 5.** (a–j) Sea surface height during one period of the wind-driven seiche in SVB with gray contour at 250 m depth. Triangles in (a) indicate the location of virtual stations A, B, and C for which time series (k) and frequency spectra (l) are shown. Maximum SSH variations occur near station A, and most energy is concentrated at a frequency of 5.2 cpd (4.6 hr). Black line in (f) corresponds to the distance used as length of the bay to estimate the theoretical period of the seiche (4.4–5.6 hr) that closely matches the dominant frequency found in the spectra.

case, but the contribution from the domain is not always larger. In fact it is smaller, on average (Figure 4g), providing evidence that stratification enhances energy transport from the bay into the domain.

The sPE induced by the SVB, calculated from the difference of SSH between the SVB run and the noSVB run, is two orders of magnitude smaller than KE, and it is dominated by the SSH response in the bay (green line vs. purple line in Figure 4f). The relative contributions to sPE from the SVB and the rest of the domain vary in time due to its oscillatory nature, but, on average, the bay contributes 74% of the sPE and the rest of the domain 26%. During the first day, these contributions are 84% and 16%, respectively, and they evolve to 72% and 28% by day 5, respectively, showing that sPE is also transferred from the bay into the domain. In the barotropic case, the contribution from the bay is slightly larger than in the stratified case with 88% on the first day and 82% by day 5, suggesting that less sPE is transferred from the bay into the domain in the absence of stratification.

### 3.3. Response to the Wind Within the Bay

As wind stress increases, water bulges close to the coast, with the largest SSH increase happening at the southeast coast of the SVB, accumulating potential energy. After the wind forcing stops, the stored potential energy transforms into kinetic energy, as a seiche mode moving counterclockwise around the bay, northward to 29°N and then decreases, transforming into a negative perturbation that moves south of 28°N, and becomes positive to start the cycle again (Figures 5a–5j). This cycle has a period of roughly 4.5 hr (see also Movie S1).

SSH at three coastal stations around the bay (Figure 5k) shows that the largest amplitudes occur in the southeastern region of the bay (station A) and that SSH oscillations are significantly smaller on the northern boundary of the bay (station C).

The seiche is mostly damped due to energy loss through radiation of waves at the mouth and form drag since bottom friction is negligible in the model configuration (Cerrovečki et al., 1997; Parsmar & Stigebrandt, 1997). At all three stations, amplitudes fall to 50% of their initial maximum values at similar rates (9.0 hr at station A, 9.2 hr at station B, and 8.8 hr at station C). The further decrease to 25% of the initial value occurs at different



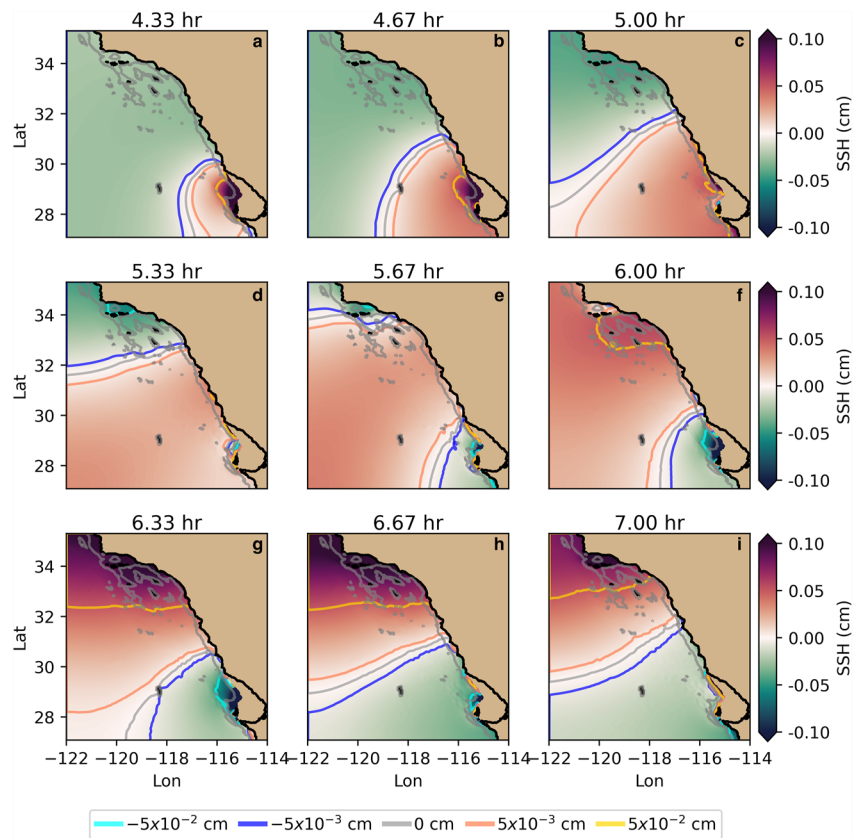


**Figure 6.** SVB-induced SSH (SVB–noSVB) from hours 4.3 to 7 shows the propagation of a gravity wave radiating from the bay (colormap and selected contours). The amplitude of the wave increases at the SCB (e.g., hour 6) and is maximum at the SBC (hours 6.3 to 7). The appearance and evolution of the yellow contour suggest that the wave is reflected at the point where the coastline bends toward the west.

rates depending on location: at station A, amplitudes fall to 25% of their initial maximum after 19.3 hr, while at stations B and C the decay time is 50% longer, requiring 28.5 hr to drop to 25% of the initial amplitude. The seiche attenuation is driven by kinetic energy loss due to form drag and radiation of waves at the bay's mouth.

Stratification increases the attenuation of the seiche. The presence of vertical density gradients provides a pathway for energy to leak from the seiche into the domain in the form of internal gravity waves (Cerrovečki et al., 1997; Cushman-Roisin et al., 2005; Parsmar & Stigebrandt, 1997), as we will show in Section 3.7. Internal waves are generated at the mouth of the bay due to the abrupt change in depth. In the barotropic case, when a surface wave in the bay travels outward, near-total reflection happens at the abrupt depth change at the mouth, but in the presence of stratification, transmission is possible via baroclinic waves into the deep ocean (Parsmar & Stigebrandt, 1997). This means that outward radiation of energy from the seiche occurs in the form of internal waves (a baroclinic-wave drag). This energy leakage has been shown to be significantly more important than bottom friction in damping the surface seiche (Cushman-Roisin et al., 2005; Parsmar & Stigebrandt, 1997).

Amplitude spectra of SSH time series around the bay show that the energy of surface oscillations is mostly concentrated at a frequency of  $5.2 \pm 0.1$  cpd (period  $4.6 \pm 0.1$  hr), in agreement with the period of the seiche cycle illustrated in Figures 5a–5j. Some energy is also present at a higher frequency peak at  $10.8 \pm 0.1$  cpd. Peaks at the same frequencies appear in the frequency spectra for the AugTS and barotropic runs, although the latter contains more energy than the stratified cases, given that it erodes more slowly (not shown).

Compared to the base run (FebTS), the barotropic run shows the same maximum initial SSH perturbation, but amplitudes decay more slowly since form drag and the radiation of surface waves are the only dissipative processes eroding the seiche. For example, it takes 110 hr for oscillations to decrease to 25% of the maximum initial amplitude at station A. That is, stratification changes the attenuation of the seiche, but not the initial excitation (not

shown), as might be expected due to shallowness at the bay. However, according to Cushman-Roisin et al. (2005), for a two-layer flow, we would expect a seiche frequency difference between baroclinic and barotropic runs proportional to  $(\rho_2 - \rho_1)^{1/2} / \rho_2$ , where  $\rho_2$  and  $\rho_1$  are the densities of the lower and surface layers, respectively. In our case, the mixed layer has a mean density of  $1021.3 \text{ kg m}^{-3}$  and the density at the mean depth of the bay ( $\approx 90 \text{ m}$ ) is about  $1022.0 \text{ kg m}^{-3}$ , so we would expect a shift in seiche frequency of 0.06% or 0.003 cpd with respect to the seiche frequency of 5.2 cpd.

We calculate the expected period of the seiche by approximating the SVB as a semi-circular or ellipsoidal bay with an exponentially decaying bottom, for which the period of the lowest mode (Helmholtz mode) is given by (Rabinovich, 2010, Chapter 11):

$$T_0 = 2.2 \frac{2L}{(gh)^{1/2}}, \quad (2)$$

where  $L$  is the distance from mouth to coast,  $h$  is the depth at the mouth, and  $g$  is the gravitational acceleration. We estimate  $L = 133.7 \text{ km}$  which is the distance from the location of maximum-amplitude SSH oscillations, close to virtual station A, to the “mouth”, chosen based on the location of an SSH-oscillation node (black line in Figure 5f). Since the bottom profile of the bay is not exponentially decaying we bound the estimation of  $T_0$  by considering two depths:  $h_{\text{max}} = 150 \text{ m}$ , the depth at the deeper end of the length  $L$ , and  $h_{\text{mean}} = 90 \text{ m}$ , the average depth along the transect  $L$ . Using these depths, the theoretical estimation of the seiche period is between 4.4 and 5.6 hr, which is in agreement with the dominant frequency of 5.2 cpd, a period of 4.6 hr, found at the virtual stations around the bay.

### 3.4. SVB-Induced SSH Variations in the Domain

Since we are interested in the response of the bay to wind forcing and its impact on the variability of SSH and vertical velocity in the domain, we subtract the results of the noSVB run, where the coastline has been modified to “erase” SVB (dashed, brown line in 1). In the following, unless otherwise stated, we consider only this difference (SVB run–noSVB run).

First, we investigate the evolution of SSH outside the SVB. At 3.5 hr, right after the wind forcing stops, a gravity wave radiates from the bay (Figure 6). Following the node (zero-amplitude contour) of the first wave that leaves the bay (gray contours in Figure 6), we can see that the wave propagates radially away from the bay (Figures 6a and 6b). Then it is refracted, as it moves faster in deeper water, and travels approximately parallel to the coast (Figures 6c and 6d) until it encounters the complex topography of the SCB, where it is further refracted, modified and scattered (Figures 6e and 6f). The topographically-induced refraction and the bend in the coast focus the wave toward the northern edge of the SCB. After the node reaches the coast, the wave is reflected at the coast and amplified in the SCB (e.g., yellow contour, Figure 6g). As the reflected wave moves radially away from the SCB, SSH amplification increases and extends in every direction, reaching its highest value at the SBC (Figure 6g–6i). Simultaneously, radiation of gravity waves from the SVB continues (Figure 6e–6i), and reflected and incident waves briefly interact at the center of the domain (e.g., Movie S1). More complex refraction patterns arise when the node reaches the complex topography of Santa Rosa Ridge and adjacent islands within the SCB. Here, in addition to bathymetric refraction, islands block and deform the wave, and the shape of the coastline causes the wave to impact the coast non-uniformly.

The propagation of the first node that leaves the SVB after the wind forcing stops, from the SVB until it reaches the SBC, is shown in Figure 7b. The shape and spacing between consecutive contours allow us to clearly see the faster phase propagation in deeper water as well as the bathymetric refraction at the slope between the 3,000 and 2,000 m isobaths and at the continental slope. Since the wave propagates at different speeds and directions across the domain, we broadly estimate the phase speed considering three regions: where the depth is 3,000 m to the west of the SVB, where it is 3,000 m to the northwest of the SVB, and where the depth is 2,000 m to the north-northwest of the SVB (color lines in Figure 7b). Considering the distance traveled by the 1st node, illustrated by the colored lines between black contours, and noting that the time elapsed between each contour is 10 min, we calculate that the phase speed in each region is  $127.4 \text{ m s}^{-1}$  ( $458.8 \text{ km hr}^{-1}$ ) in the deepest part to the west of the SVB,  $204.2 \text{ m s}^{-1}$  ( $735.3 \text{ km hr}^{-1}$ ) to the northwest of the SVB and  $90.6 \text{ m s}^{-1}$  ( $326.2 \text{ km hr}^{-1}$ ) in

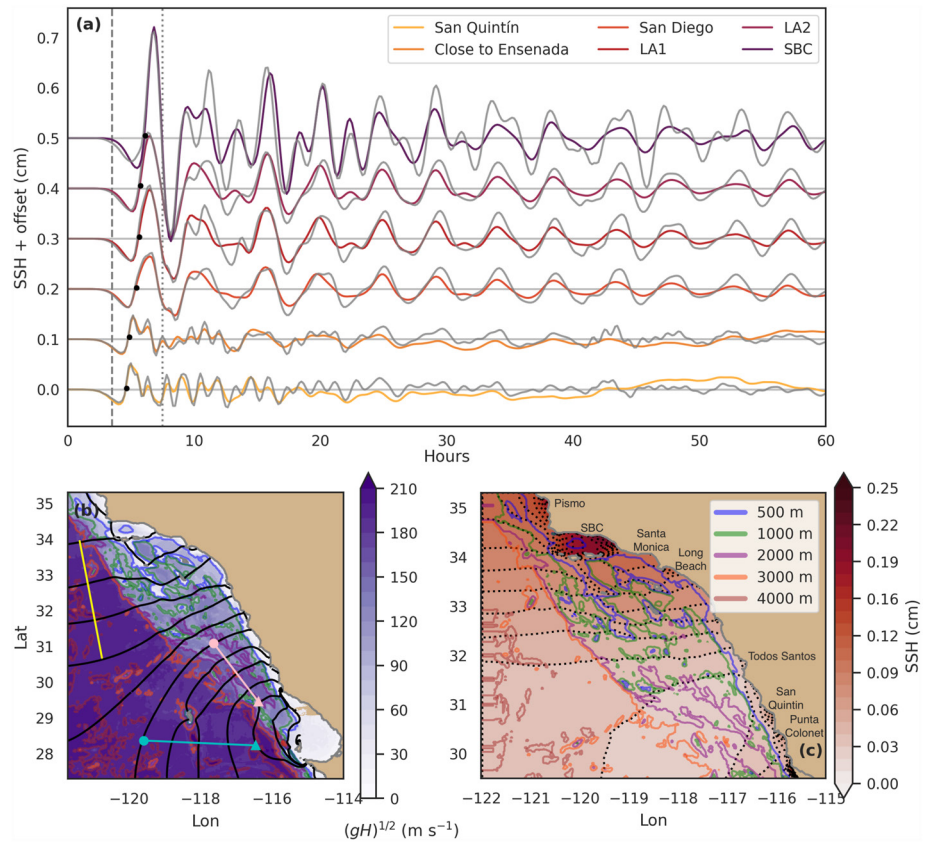


**Figure 7.** (a) Time series of SVB-induced SSH (SVB–noSVB) at key stations along the coast shows that SSH is amplified as we move away from the bay. The attenuation of oscillations for the barotropic run (gray lines). The dashed, vertical line marks the end of wind-stress forcing, and black dots indicate the first zero-crossing of the initial gravity wave that propagates across the domain. (b) Propagation of the first node (black contours) that leaves SVB after the wind forcing stops. The time between contours is 10 min. (c) Contours of maximum SSH reached before hour 7.5 (dotted line in a) show that SSH is amplified toward the north, in particular at the SBC. Also, at the SCB, maximum SSH contours tend to align with isobaths (solid, color contours).

the shallower part to the north of the SVB. The calculated velocities are smaller than the expected phase speed of  $(gH)^{1/2}$  closer to the SVB, and very close to the expected value farther northwest of the SVB.

The wavelength of the gravity wave is  $\lambda_1 \approx 1,493$  km in the deeper portion of the bathymetry, where the depth averages 3,000 m, and  $\lambda_2 \approx 1,080$  km in the shallower portion, where the depth averages 2,000 m (Figure S3 in Supporting Information S1). Considering the theoretical phase speeds at each depth, from Snell's Law ( $c_2/c_1 = \lambda_2/\lambda_1$ ) we expect a 20% decrease in wavelength when going from 3,000 to 2,000 m depth. Indeed, our wavelength estimates give us a 30% decrease in wavelength, which is in reasonably good agreement with Snell's law considering the complexity of the coastline and the topography that the wave encounters as it passes over the SCB.

Amplification of SSH variability at the SCB is detectable in virtual stations along the coast (Figure 7a), with maximum amplification at the SBC. This amplification is seen very clearly for the first incident wave, as well as throughout the simulation. Time series of selected stations along the coast show that the amplification can be as large as a factor of 7.5 (e.g., SBC vs. San Quintin) (Figure 7a). Without stratification, the maximum amplitude of the oscillations at the beginning of the simulation does not change, but as in the case of the seiche in the SVB, the oscillations decay more slowly in the unstratified case than in the stratified case (gray lines vs. color lines in Figure 7a). The amplification of SSH, consistent with the gravity wave bending and focusing into the coast at the SBC, is similar for the barotropic case, and there is little difference between the FebTS and AugTS runs.

The spatial structure of the amplification of SSH throughout the domain can be seen from the maximum SSH in the domain induced by the first crest leaving the bay (Figure 7c). This metric shows that there is a northern

amplification of the signal, coincident with bathymetric contours and the bend in the coast (e.g., 500 m) around the SCB, Santa Rosa Ridge, and the shelf at Point Conception. Note that there are also local maxima of amplification at the bays along the coast at San Quintin, Punta Colonet, Todos Santos Bay (Ensenada), Long Beach, Santa Monica, and Pismo.

### 3.5. SVB-Induced SSH Response Along the Coast

In order to evaluate the SVB impact on SSH along the coast, we again consider the SVB minus noSVB runs (Figures 3c and 3d). The difference in SSH reveals two main types of signals that travel north along the coast: fast barotropic signals composed of multiple frequencies (quasi-vertical stripe pattern in Figures 3c and 3d) with amplitudes that decrease after the wind forcing stops, and slower, baroclinic signals that appear after the first day of simulation (tilted positive stripes in Figure 3c).

The dominant signals during the first day correspond to the fast gravity waves radiating from the bay described in the previous section. In Figures 3a and 3b we can see again the amplification of the gravity waves as they travel north and away from the SVB, with maximum amplification at the SBC and around Point Conception (Figures 3c and 3d).

An unexpected effect of the SVB signals on SSH is the ringing of some bays along the coast, mainly San Diego, San Quintin, and Ensenada (Figure 3d). These oscillations in the bays are induced by the signals coming from the SVB since we have subtracted the natural oscillations excited directly by the wind. In general, the dominant frequency at these bays coincides with the natural frequency of SVB-induced waves (5.2 cpd, Figure S2c in Supporting Information S1), which suggests that waves directly generated at the SVB are amplified at some of the bays along the coast. Each bay oscillates in a different way. For example, at San Quintin, energy is equally distributed between 5.2, 7.6, and 17.5 cpd; Pismo and Long Beach have a large energy peak at 7.6 cpd; while Todos Santos Bay mainly oscillates at a single frequency (Figure S2c in Supporting Information S1).

Surface baroclinic signals travel along the shelf at a speed of approximately  $3 \text{ m s}^{-1}$  at latitudes between SVB and San Diego (Figure 3e–3g). Snapshots after 3.5 days of simulation of SSH, and surface meridional velocity and vertical velocity at 197 m depth show a spatial pattern along the coast that is consistent with a CTW propagating poleward. CTWs are sub inertial waves that propagate with the coast on the right (left) in the northern (southern) hemisphere and decay off-shore. They are a hybrid-type wave between internal Kelvin waves and topographic Rossby waves, with a cross-shelf modal structure determined by the cross-shelf profile of the shelf and slope, stratification, and bottom friction (e.g., K. Brink, 1991; Huthnance et al., 1986; Hughes et al., 2019). As expected, these signals do not appear in the barotropic run.

From SSH time series, the phase speed of this CTW is between  $2.7$  and  $4.9 \text{ m s}^{-1}$ , depending on the station considered, possibly dependent on shelf shape. From a linear model that solves for the allowed modes of a CTW given the cross-shelf depth profile, stratification and latitude, and assuming a uniform shelf alongshore (K. H. Brink, 2018) we calculate that the speed of the gravest mode allowed for the shelf profile between SVB and San Quintin should be  $2.9 \text{ m s}^{-1}$ , decreasing northward to  $2.0 \text{ m s}^{-1}$  around San Diego. The vertical structure and propagation of these CTWs are left to future investigations.

### 3.6. Frequency Content of SSH Variations

Frequency spectra of the SSH signal induced by the SVB along the coast reveal that most of the energy in the oscillations generated by SVB is distributed among three frequencies: 5.2 cpd, 7.6 cpd, and 10.8 cpd (Figures 8a and 8c). The first and most energetic frequency, 5.2 cpd, coincides with the natural frequency of SVB (Figure 5I); the second frequency, 7.6 cpd, appears in both SSH spectra for the full runs with and without the bay, but is more energetic when SVB is not included (Figure 8b), which suggests that it is related to the topography of the SCB; and the third and least energetic frequency, 10.8 cpd, is also associated with the bay.

The SSH amplification effect at the SBC is also seen in the power spectral density (PSD) content of each frequency peak at stations along the coast (Figure 8c). In general, the largest peak is at 5.2 cpd and the smallest at 10.8 cpd, but the relative size of peaks at different stations varies, with the largest PSD at the SBC. Relative variation of PSD between stations is largest for the 7.6 cpd peak, and it is relatively constant for the 5.2 cpd peak, which suggests that the amplification effect that occurs at the SBC is largest for the components of the signal with frequencies of 7.6 (Figure 8a). This is consistent with the hypothesis that the amplification of the wave is caused by the topographic refraction and consequent focusing due to the shape of the coastline.



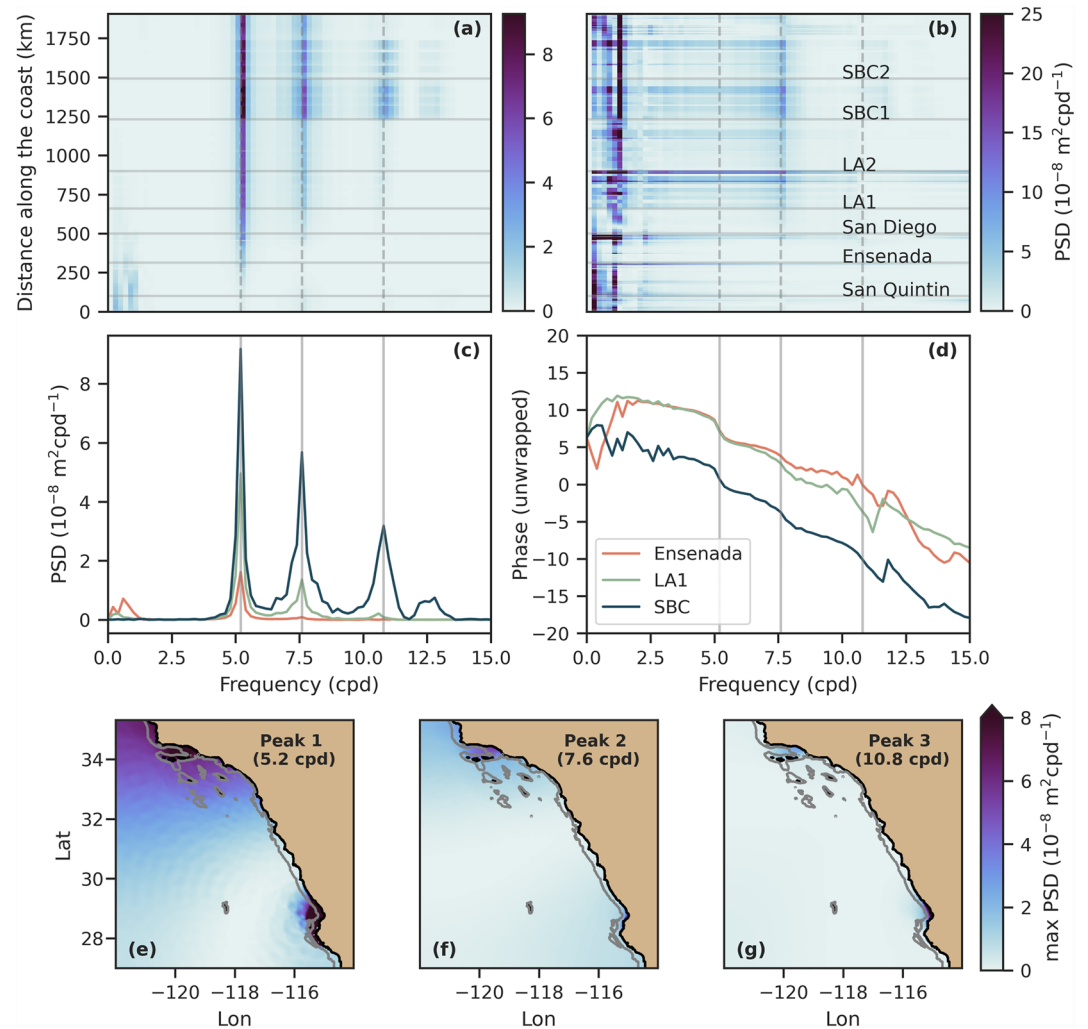


**Figure 8.** SSH frequency spectra along the coast for (a) bay-generated (SVB–noSVB) signals show three dominant frequencies: 5.2 cpd, 7.6 cpd, and 10.8 cpd, and (b) no-bay signals indicate that the 7.6 frequency peak is related to the noSVB run. (c) Frequency and (d) phase spectra of SVB-induced SSH at three stations along the coast show the amplification of PSD content in the dominant frequencies and the resonant nature of frequencies associated with SVB, respectively. (e–g) Spatial distribution of power spectral density (PSD) of bay-induced SSH at relevant frequencies of 5.2, 7.6, and 10.8 cpd. Spectra are calculated using 5 days of simulation, with output every 10 min. The frequency resolution is 0.2 cpd.

SVB-generated SSH oscillations at the three main frequencies appear to be resonances. Phase spectra for the SSH time series show sharp, step-like changes in phase at 5.2 and 10.8 cpd (Figure 8d), characteristic of resonant phenomena (Georgi, 1993). The 5.2 cpd frequency coincides with the main natural frequency of the SVB, while 10.8 cpd is also associated to the presence of the bay in the domain.

The energy distribution is robust to changes in stratification. The barotropic run and AugTS run also have frequency peaks at 5.2, 7.6, and 10.8 cpd, and the relative size of PSD between stations is consistent with focusing on the coast as a cause. However, the amplification is larger in the barotropic case (not shown).

Frequencies associated with baroclinic signals traveling along the coast can be seen close to the bay. Within 500 km of the bay, frequency spectra show a low-frequency peak (0.5–1 cpd) for the FebTS (Figures 8a and 8c) and AugTS (not shown) runs; these peaks are not present in the barotropic run spectra (not shown). The presence of these peaks within 500 km of the bay is in agreement with the spatial extent of CTW propagation in Figure 3c.

The northern amplification of SSH signals can be identified away from the coast based on the spatial structure of the dominant frequency peaks of SSH. To evaluate the spatial distribution of the SSH PSD, at each location in the domain, we identify the PSD value associated with each dominant frequency peak (5.2, 7.6, and 10.8 cpd)

(Figures 8e–8g). These maps reveal that oscillations in all three frequencies are more energetic in the SCB, and particularly so in the SBC. The smallest oscillations at 5.2 cpd take place in a ring around the bay.

The maximum energy of all peaks is smaller in the baroclinic run than in the barotropic run, in general. The maximum energy for baroclinic peak 1 is about 40% of that in the barotropic case, 70% of peak 2, and about the same for peak 3. In a few locations, the baroclinic energy is larger, but this only happens in regions where the maximum energy of the peaks is very low (Figure S4 in Supporting Information S1).

### 3.7. Effect of SVB in the Ocean Interior

The discussion so far has focused on SSH. Below the surface, the effect of the bay can be identified in the form of IWs radiating away from the bay (Figure 3g and Movie S2), which explains why barotropic oscillations such as the seiche in SVB decay faster for the stratified runs. The IW field induced by the SVB is generated in two ways: IWs that are generated directly at the bay and radiate away from SVB; and IWs excited by the gravity wave propagating over regions of rough topography such as the Santa Rosa Ridge (Movie S2). At the beginning of the simulation (hours 3.5–5), IWs radiate from the SVB, and from prominent features of the topography and the coastline. These waves propagate away from their generation points and interact with each other. As the simulation progresses, IWs generated at the abrupt topography decay, and, by hour 70, IWs radiating from the bay permeate the whole domain, given that the seiche keeps providing energy for their generation. There are only three regions where there is no IW activity: at the northern SCB close to where the coastline bends to the west, where IWs seem to have dissipated or scattered; within the shadow generated downwind of Guadalupe Island, and along the coast, where the CTW dominates the vertical velocity signal (Movie S2).

IWs can be seen outside the bay starting at 3.5 hr, at about the time when the wind stops blowing over the bay, faintly at first and clearly after 5 hr (Figure 9a, station A in Figure 1). We calculate the vertical displacement  $\Delta h$  that a water parcel in the water column would undergo by integrating the vertical velocity at every depth throughout the simulation (i.e., the cumulative sum of  $w\Delta t$  at every depth in the water column). Vertical displacements ( $\Delta h$ ) induced by the IWs are maximum at 500 m with maximum magnitudes around 7 cm. This is also the case for vertical velocities, with maximum values around  $1.3 \times 10^{-5} \text{ m s}^{-1}$  (Figure S5a in Supporting Information S1). Given the vertical uniformity of the wave structure, the maximum could be explained by a combination of low stratification at 500 m and being sufficiently separated from the bottom. Compared to any of the other regions in the domain (stations B, C, and D), station A has larger displacements and an order of magnitude more vertical velocity variability. The signals in vertical displacement and velocity decay in time, but can be identified until the end of the simulation. This can also be seen from time series of  $\Delta h$  at 200 and 500 m (Figure 10a).

Further north and away from the shelf, at station B, IWs arrive after 3.5 hr, with vertical displacements reaching their maximum values around hour 20 and below 500-m depth (Figure 9b). Vertical displacements above 500 m decay after 20 hr, but the  $\Delta h$  signal at 1,000 m seems to increase its period and reach its maximum absolute values of 4.3 cm after about 55 hr. This can also be seen in the vertical velocity structure shown in Figure S5b in Supporting Information S1. The apparent increase in period can also be seen at 200 and 500 m depth time series of  $\Delta h$ .

At station C, above the complex topography at the entrance of SCB, a shorter pulse of IWs appears after only 3.5 hr. Given that this wave packet is generated soon after the wind forcing stops, and that IWs cannot travel as fast as the gravity wave, this suggests that the wave packet is locally generated. This can be corroborated in Movie S2 and Figure S5c in Supporting Information S1. The structures of  $\Delta h$  (Figure 9c) and  $w$  (Figure S5c in Supporting Information S1) suggest upward propagation, displacements of 0.5 cm, and velocities of  $2.3 \times 10^{-6} \text{ m s}^{-1}$  occurring close to 500 m, but the locations of the maximum  $\Delta h$  and  $w$  in the water column vary. Vertical displacement variability decreases much faster than at stations A and B, possibly due to enhanced dissipation at the topography (Figure 10c).

Finally, at station D in the open ocean, IW activity starts after 3.5 hr, with a clear arrival of the main wave packet after hour 30 and a subsequent decrease in variability. Here, the vertical structure of the waves is uniform below 500 m, and maximum displacements of 0.5 cm occur below 1,000 m (Figure 9d). This coincides with the maximum stratification changes occurring in the first 200 m of the water column and almost constant densities below 500 m.

Frequency spectra of vertical displacement at 500 and 200 m show that  $\Delta h$  variations occur at 5.2, 7.6, and 10.8 cpd, coincident with the main frequencies of variability of SSH (Figures 10e and 10f). The match between dominant frequencies for SSH and  $\Delta h$  suggests a pathway for energy moving from the wind, to the bay and into

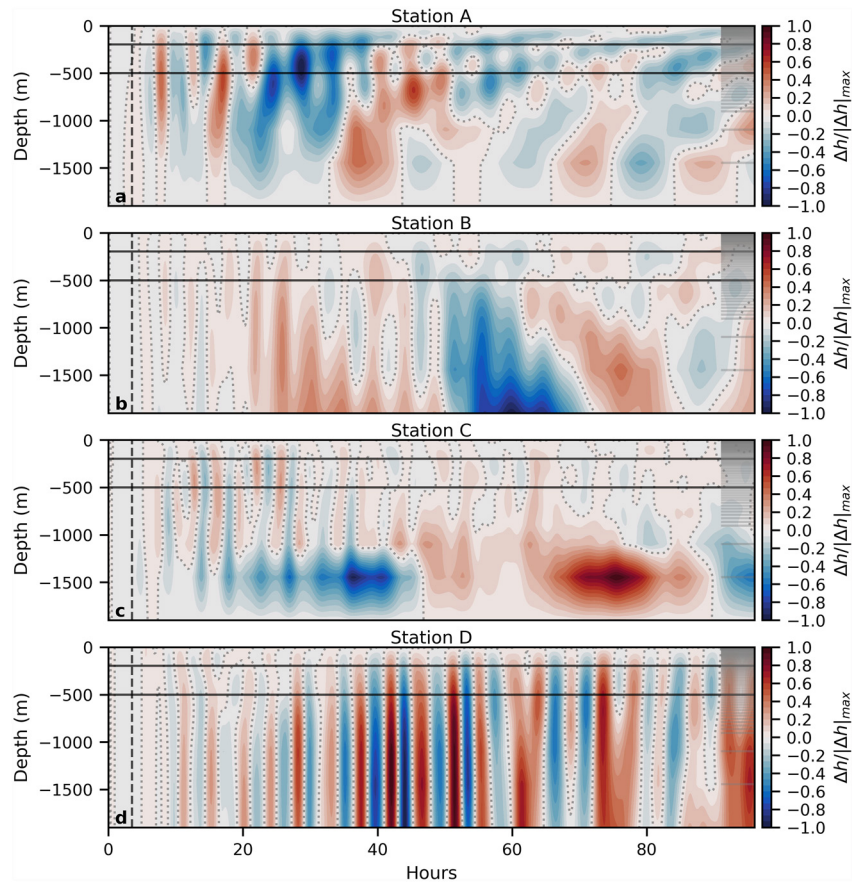


**Figure 9.** Hovmöller plots of SVB-induced vertical displacement,  $\Delta h$ , at stations A-D (indicated in Figure 1) for the first 4 days of simulation. Vertical displacement at station A, outside SVB, can be 8 times higher than at other stations, so  $\Delta h$  is shown here normalized by the maximum of the absolute value of  $\Delta h$  to highlight the vertical structure and temporal variations at each station. For reference, the maximum values of  $|\Delta h|$  at stations A-D are 7.5, 4.3, 1.5 and 0.5 cm, respectively. The two horizontal lines at 200 and 500 m indicate where time series in Figure 10 are taken; the vertical, dashed line indicates the end of the wind-stress forcing, and the short, horizontal lines on the right side of each panel show the depth of the vertical levels in the output (more levels were modeled).

the domain in the form of IWs. The dominant frequency is 5.2 cpd outside the bay (station A), off-shore the Baja coast (station B), and in the open ocean (station D), but not at the region with complex topography (station C), where the dominant frequency is 7.6 cpd. This is more evident at 500 m. Outside the bay, the peak at 10.8 cpd is more energetic than the 7.6 cpd peak, which is not as clearly defined as for stations C and D. Station B shows a mixture between the spectra at A and at C. This area seems to be a transition zone between the region dominated by SVB and the SCB, dominated by the 7.6 cpd oscillations. The energy at near-inertial frequencies—with a period of about 1 day in these latitudes—outside the bay and off-shore Baja California at both 200 and 500 m is as significant as that at 5.2 cpd. These regions coincide with the areas of influence of the northward propagating CTWs, for which we estimated a period of about 1 day.

Although the stratification below 100 m is almost identical in the AugTS and FebTS runs, there are some differences in the vertical structure of internal waves near the SVB between 0 and 500 m (e.g., station A, Figure S9 in Supporting Information S1). Time series at 200 and 500 m are very similar in both cases, but the August-like stratification run tends to have slightly larger vertical velocities (Figure S10 vs. Figure S6 in Supporting Information S1). Regarding their contribution to the internal wave spectra, we find that there is no clear pattern as to which one has larger values of PSD at the relevant frequencies (near inertial, 5.2 cpd, 7.6 cpd and 10.8 cpd), but near the bay maximum PSD values at 5.2 cpd (related to the bay) are  $2.27 \times 10^{-11} \text{ m}^2 \text{ s}^{-2} \text{ cpd}^{-1}$  ( $1.52 \times 10^{-4} \text{ m}^2 \text{ cpd}^{-1}$ ) for the August stratification and  $3.35 \times 10^{-11} \text{ m}^2 \text{ s}^{-2} \text{ cpd}^{-1}$  ( $2.27 \times 10^{-4} \text{ m}^2 \text{ cpd}^{-1}$ ) for the February stratification, both at 200 m; while at 500 m we get  $2.27 \times 10^{-11} \text{ m}^2 \text{ s}^{-2} \text{ cpd}^{-1}$  ( $8.50 \times 10^{-5} \text{ m}^2 \text{ cpd}^{-1}$ ) for the August

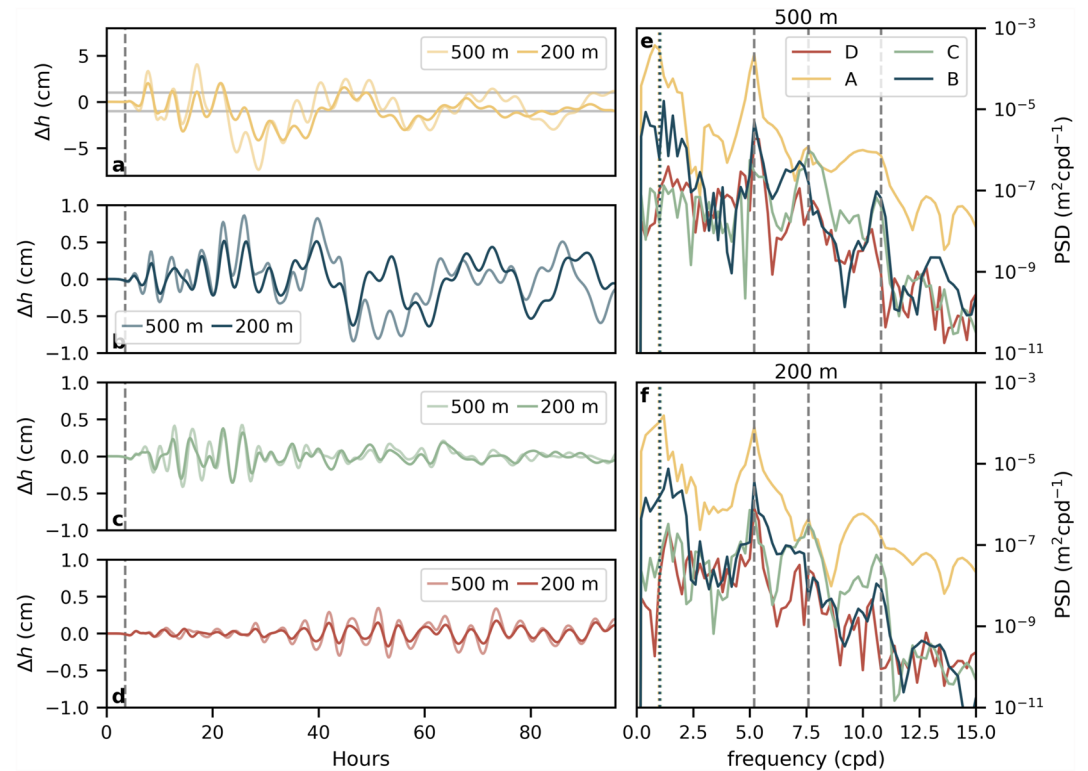


**Figure 10.** (a–d) Time series of vertical displacement at 200 and 500 m depths at stations A–D, with locations indicated in Figure 1, during the first 4 days of simulation. Note that solid gray lines in panel a indicate the y-axis limit in panels b–d. The frequency spectra of these time series (e, f) exhibit peaks at 5.2, 7.6, and 10.8 cpd (dashed, vertical lines), although their relative importance is different at each location. The dotted vertical line indicates the inertial frequency at each station. Spectra are calculated using 5 days of simulation, with output every 10 min. The frequency resolution is 0.2 cpd.

stratification and  $1.26 \times 10^{-11} \text{ m}^2 \text{ s}^{-2} \text{ cpd}^{-1}$  ( $8.08 \times 10^{-5} \text{ m}^2 \text{ cpd}^{-1}$ ) for the February stratification (Figures 10, Figures S6, S8, and S10 in Supporting Information S1). This is consistent with the fact that, locally, the stratification is larger at 200 m for the FebTS run ( $0.0071$  vs.  $0.0069 \text{ s}^{-1}$ ), while at 500 m, stratification is slightly larger in the AugTS run ( $0.0036$  vs.  $0.0037 \text{ s}^{-1}$ ).

SVB-induced vertical velocity variance ( $w^2$ ) at depths below 200 m, calculated after 2 days of simulation, show that the area outside the bay, Santa Rosa Ridge and the adjacent islands in the SCB, and isolated islands such as Guadalupe Island are regions of relatively larger variance than the rest of the domain, suggesting that these may be hot spots where IWs generated near SVB are interacting with the complex topography (Figure 11a–11c).

In the runs both with and without the SVB, mean vertical velocity variance per depth is maximum after 1 day and decreases as the oscillations in the domain are attenuated (not shown). The presence of the bay increases the mean  $\langle w^2 \rangle$  by 15%–27.5% with respect to the run without the bay after day 1 at depth levels between 100 and 500 m depth (Figure 11c). This mean depth-level enhancement decreases in time to 8%–10% after day 5; increasing the stratification above 200 m (AugTS vs. FebTS) reduces this effect because the enhanced stratification inhibits the amount of available potential energy. In the barotropic case, there is a small quasi-constant enhancement of about 5% due to topographically induced variations of  $w$ .

#### 4. Discussion

To our knowledge, this is the first study to describe the structure of the seiche in SVB and its natural frequency. Seiche decay due to baroclinic wave-drag like in the SVB has been observed in the Adriatic Sea (Cerrovecchi et al., 1997) and the Gullmar Fjord in Sweden (Parsmar & Stigebrandt, 1997), to name a few, and in laboratory experiments (e.g., Medjdoub et al., 2021). In both geographical cases, bottom drag could not account for the observed barotropic seiche decay, while a baroclinic wave drag due to internal wave generation at steep topography



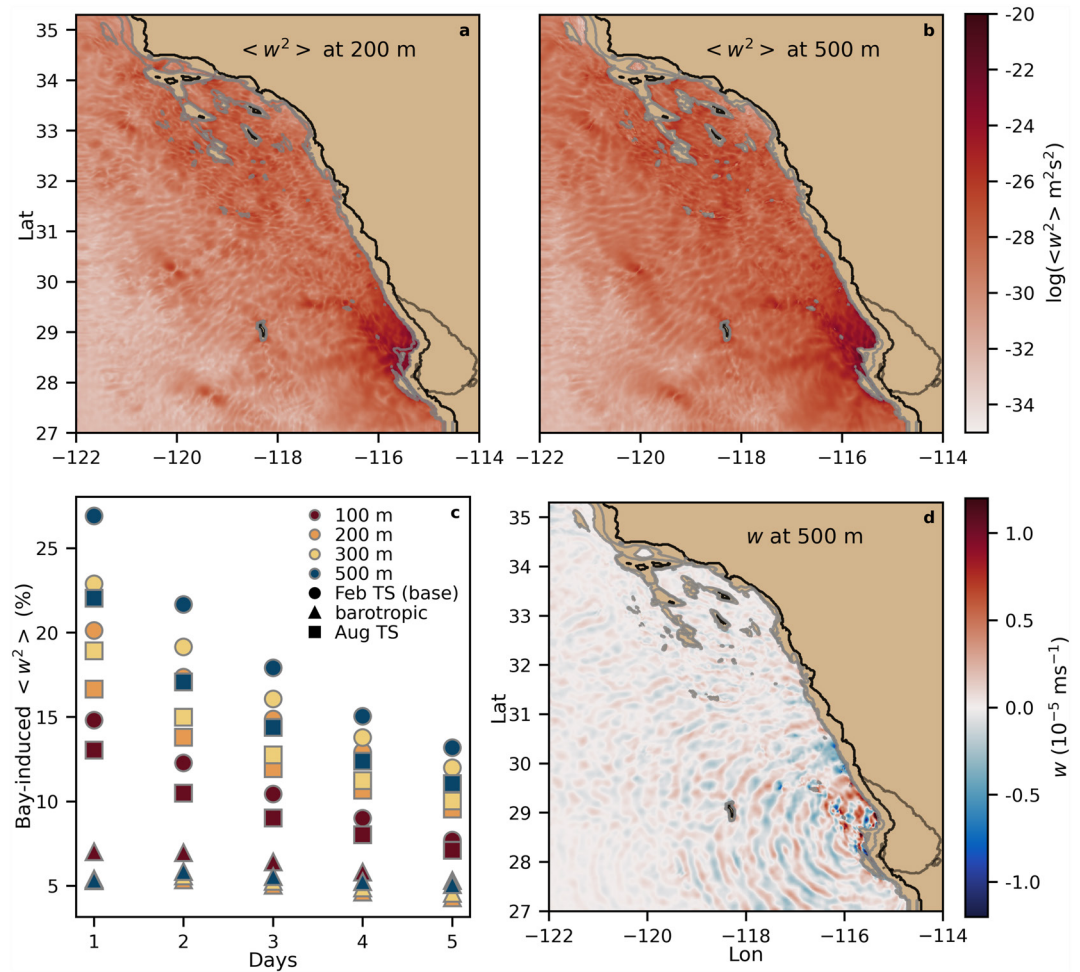


**Figure 11.** Vertical velocity variance  $\langle w^2 \rangle$  induced by the SVB, calculated after 2 days of simulation at (a) 200 m and (b) 500 m is enhanced near Santa Rosa Ridge and neighboring islands as well as around SVB. (c) Difference (%) in area-weighted  $\langle w^2 \rangle$  average at different depths between runs with the SVB and without the SVB shows that the presence of the bay increases  $\langle w^2 \rangle$  in the domain by up to 27% on the first day and up to 15% by day 5 for the base case. (d) A snapshot of vertical velocity  $w$  induced by the SVB at 500 m on day 2 shows IWs propagating away from the SVB and away from the rough topography of Santa Rosa Ridge and neighboring islands.

at the mouth was a viable mechanism to account for most of the decay. In the case of the laboratory experiments, an analogous system to semi-enclosed stratified basins is represented by a quasi-two-layer flow separated by an obstacle at the bottom or a “sill.” In this model, again, internal waves generated at the sill via topography-induced baroclinic wave drag contribute considerably to seiche damping. So, this mechanism of IW generation is not only expected to occur at SVB with each wind event, but also to be ubiquitous at any semi-enclosed coastal feature.

In this study, we have found that after a short wind event (<4 hr) the SVB becomes a continuous source of surface gravity waves, IWs, and CTWs to the North Pacific coast of Baja California and to the Southern California Bight (Figure 12). These wave responses explain the connection found by Verdy et al. (2014) between SSH variability in Port San Luis and winds blowing over SVB. The findings quantify the variability excluded from regional models that omit the SVB.

The gravity waves induced by any individual wind event have only a small impact on SSH variability, and IW variance decays within 2 days after the termination of a wind event. However, the cumulative effect is large, as there are O(100) wind events of similar magnitude and duration over the SVB every year, as shown in Section 2 for 2016. The 76 wind events close to the southwest boundary of the bay (Figure 2) have a mean duration of 5.4 hr, a standard deviation of 5.4 hr, and a mode of 1 hr. Assuming 2016 to be a typical year, the SVB enhances

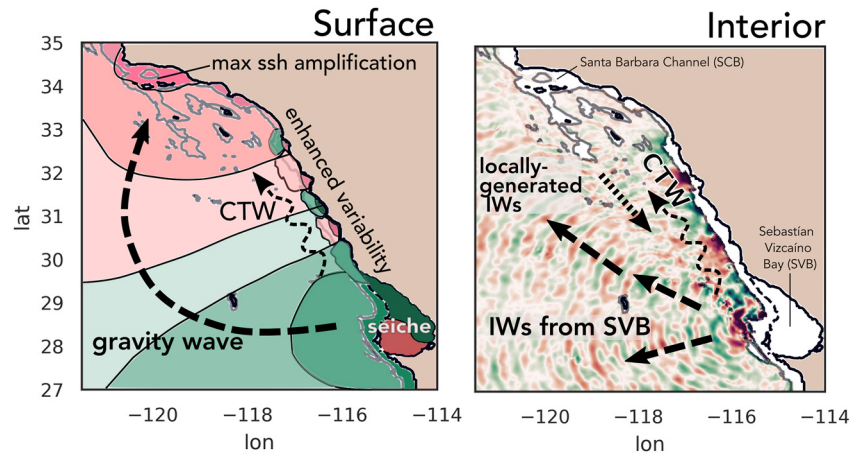


**Figure 12.** Schematic of SSH (surface) and vertical velocity  $w$  (interior) response induced by a wind burst over SVB. Pink and green colors correspond to positive and negative perturbations of either SSH or  $w$ , respectively. All colored regions oscillate between positive and negative at different frequencies, depending on the nature of the oscillation. Darker hues indicate larger amplitudes. Because the SVB is semi-enclosed, a single burst of wind generates a seiche mode at its resonant frequency, of 5.2 cpd. As the seiche energy dissipates, it leaks energy into three forms. First, shallow water gravity waves propagate rapidly away from the coastline with a phase speed  $(gH)^{1/2}$ . As these waves pass coastal bays and inlets, they excite seiche modes with different resonant frequencies. Second, baroclinic signals travel northward along the shelf at a speed that is consistent with CTWs. Third, IWs radiate away from the bay in all directions, filling up the entire model domain. The presence of the SVB is responsible for higher vertical velocity variance and thus the opportunity for greater vertical mixing throughout the SCB and especially in the SBC, at the northern end of the SCB near Santa Barbara.

vertical velocity variance every few days, mainly in spring, fall, and winter, when we found the largest impact in vertical velocity variance (FebTS).

While the SVB alone would not be expected to contribute much to the total IW energy budget throughout the global ocean, the impact of the collection of all equivalent coastal features across the planet may be significant and could play a role in shaping the structure of the Garrett–Munk spectrum. From the PSD in Figure 10 we find that a single wind event contributes on the order of  $1 \times 10^{-4} \text{ m}^2 \text{ cpd}^{-1}$  at a frequency of 5.2 cpd. Multiplied by 100 events per year that is a total of  $1 \times 10^{-2} \text{ m}^2 \text{ cpd}^{-1}$  per year. The vertical displacement Garrett–Munk frequency spectrum (GM76) at a frequency of 5.2 cpd predicts  $2.0 \text{ m}^2 \text{ cpd}^{-1}$  at 200 m depth and  $3.5 \text{ m}^2 \text{ cpd}^{-1}$  at 500 m depth, considering a mean latitude of  $31.5^\circ$  and local stratification values of  $N_{200\text{m}} = 6.9 \times 10^{-3}$  and  $N_{500\text{m}} = 3.6 \times 10^{-3}$ , calculated using the MATLAB toolbox created by Klymak (2017). Although the SVB-induced variability is two orders of magnitude smaller than the GM76 prediction, thousands of bays around the world with similar configurations may be continuously contributing with bursts of IW energy. Some aspects to consider about this estimate are that the highest values of PSD ( $O(10^{-4} \text{ m}^2 \text{ cpd}^{-1})$ ) are observed closer to the bay, which suggests that the total contribution in the global GM spectrum would be smaller, given that the effect is enhanced mainly closer to the bay, suggesting a more regional effect. On the other hand, our time series are 5 days long, but the forcing only lasts 3.5 hr. If wind events happen back to back or with larger magnitudes than the one simulated here, the corresponding spectra may have a higher PSD for the same time period of 5 days, in which case the estimate may be applied more globally. From our results, we hypothesize that energy moves from the wind to the seiche, to the barotropic gravity wave, and into the IW spectrum. This topography-wave interaction could be one pathway to force the Garrett–Munk spectrum in the higher frequencies.

The amplitude of the high-frequency oceanic response induced by the bay is small ( $\sim 1$  cm) compared to other processes such as tides, surges, or waves. However, the high-frequency small-amplitude variations analyzed here (5.2 cpd or a period of 4.6 hr) are captured by bottom pressure sensors routinely used by geophysicists. For example, basin-mode oscillations in the Japan East Sea, with amplitudes and periods similar to oscillations generated by the SVB (SSH variations of  $O(1 \text{ cm})$  and dominant period of 6.7 hr) have been identified using tide gauge and bottom pressure data (Xu et al., 2007). In fact, there is a growing interest in understanding oceanographic processes at timescales ranging from a day to a month that may affect bottom pressure measurements in order to remove the oceanic signal to obtain a “cleaner” analysis of geophysical processes (e.g., Dobashi & Inazu, 2021;

Watts et al., 2021). Even though the timescales of interest are longer than those analyzed here, these signals have sufficient SSH variability, and long enough periods in the case of the generated CTWs, to mask the geodesic signals.

The bay allows more energy into the ocean. The simulation with the SVB receives 3% more wind energy than the simulation without the bay because there is a 3% larger ocean surface. We estimated that this translates into a 3.4% increase in the maximum KE that the model develops right after the forcing stops, so the coastal structure can affect wind energy input beyond the change in surface area. From this additional wind energy input, we saw that the largest energy changes with respect to the noSVB run occur in the bay itself, with KE in the SVB accounting for 85% of the total change in KE, and sPE in the SVB accounting for 74% of the total sPE change by day 5. The residual contributions, which correspond to the effect of the bay in the rest of the domain, represent 15% of the total increase in KE and 26% of the total increase in sPE, showing that the SVB serves as a pathway for wind energy into the rest of the domain. To add further context, the volume of the SVB is only 0.2% of the total volume of the domain considered here, and yet it non-negligibly affects the energy pathways from the wind into the domain. We should also consider that adding bottom friction to the simulations reduces the maximum amount of energy available to radiate out of the bay.

## 5. Summary and Conclusions

This study has investigated how an isolated wind event over one large bay, the SVB, can have a far-reaching impact, extending northward along the Mexico-California coastlines from the northern half of Baja California to Santa Barbara. We have carried out simulations with and without the SVB in order to quantify its impact. Because the SVB is semi-enclosed, a single burst of wind readily generates a seiche mode at its resonant frequency, approximately 5.2 cpd. As the seiche energy dissipates, it leaks energy in three forms (Figure 12).

First, shallow water gravity waves propagate rapidly away from the coastline with a phase speed  $(gH)^{1/2}$ . As these waves pass coastal bays and inlets, they excite seiche modes with different resonant frequencies, resulting in variability at additional frequencies.

Second, baroclinic signals travel along the continental shelf at a speed that is consistent with CTWs traveling northward along the coast with a phase speed almost two orders of magnitude slower than the gravity waves.

Third, IWs radiate away from the bay in all directions, filling up the entire model domain. The presence of the SVB is responsible for higher vertical velocity variance and thus the opportunity for greater vertical mixing throughout the SCB and especially in the SBC, at the northern end of the SCB near Santa Barbara. However, it is possible that in some regions the potential enhancement of mixing due to the presence of the SVB may be negligible compared to the levels of tidally driven mixing.

These results underscore the importance of representing coastal topographic features as well as the wind driving coastal regions in order to represent the processes responsible for high-frequency variability and turbulent mixing in the global ocean.

In this work we only explore the effect of a horizontally homogeneous stratification and uniform wind forcing, and we do not include forcing at the boundaries such as tides. However, the comparison between bay and no bay runs helps us to isolate effects that otherwise would be buried in the variability of more energetic processes in the ocean. Future work will explore the effect of the SVB after restarting from the ocean state estimation for the CCS, the California Estate Estimate (CASE project), which would provide a realistic spatial distribution of temperature and salinity.

The importance of remote forcing in the SCB has been identified in several temporal and spatial scales (e.g., Dong et al., 2009; Durazo, 2015; Gómez-Valdivia et al., 2017; Hickey et al., 2003). Here we find that the SVB seiche is a source of SSH and vertical velocity variability into the SCB at super inertial frequencies, through the generation and radiation of gravity waves and internal waves, and, at approximately diurnal frequencies, through the generation of CTW's. A detailed characterization of the propagation and structure of CTW signals will be the subject of a separate study.

More work is needed to characterize the IWs in the model and their fate in the SCB. The main question that we suggest should be addressed is whether they can be measured in available moorings and other instruments, and

what might be their contribution to mixing in the region. The current configuration cannot answer the latter. Moreover, in preliminary runs, we noticed that the smoothness of the bathymetry input to the model can make a difference in the IW structure. Future work will investigate how IWs in the model are affected by the level of smoothing applied to the bathymetry and bottom friction parametrizations.

Finally, this study has provided evidence that the coastline and coastal topography may enhance the amount of energy transferred from the wind into the ocean, increasing oceanic variability. Future work will explore the effect of the coastline more systematically and will attempt to quantify this contribution.

## Appendix A: Energy Contributions

We calculate the wind power input per unit area as

$$P = \vec{u}_s \cdot \vec{\tau}, \quad (\text{A1})$$

where  $\vec{u}_s$  is the surface velocity and  $\vec{\tau}$  is the wind stress. Then, an integral of  $P$  over area gives a flux of energy in J/s, and integration over time gives us the total energy input in J (e.g., Duhaut & Straub, 2006).

Potential energy can be divided into available potential energy and “barotropic” potential energy, or the potential energy associated with changes in SSH. We consider only the latter, calculated as:

$$sPE(t) = \frac{1}{2} \iint \rho_0 g [H - H_0]^2 dx dy = \frac{1}{2} \iint \rho_0 g \eta^2 dx dy, \quad (\text{A2})$$

where  $H_0$  is the reference depth,  $H$  is the depth of the water column,  $\eta = H - H_0$  is the free surface,  $\rho_0$  is a constant reference density, which was chosen as the average of the initial density profile (e.g., Vallis, 2017).

Finally, kinetic energy in the domain was calculated as

$$KE(t) = \frac{1}{2} \iiint \rho (u^2 + v^2 + w^2) dx dy dz, \quad (\text{A3})$$

where  $\rho = \rho(x, y, z, t) = \rho_{\text{anoma}}(x, y, z, t) + \rho_{\text{ref}}(z)$  from model output.

Volume integrals as well as surface integrals were done over the whole domain to calculate KE in the SVB and noSVB runs. To isolate the contributions from the SVB to the domain and in the bay itself we calculated sPE and KE in two ways. First, the effect of SVB in the domain was calculated by subtracting the dynamic fields (SSH,  $u$ ,  $v$ ,  $w$ , etc.) of the SVB run and the noSVB run, and considered only the domain without the bay in the integrals (noSVB land mask). Second, the total effect of the SVB over the full model domain was calculated as before, but integrating over the bay and the rest of the domain (using the SVB land mask). Finally, the contribution of the bay's region was calculated by subtracting the two aforementioned contributions.

## Data Availability Statement

The model results are available at Zenodo via DOI: <https://doi.org/10.5281/zenodo.7933674> (<https://doi.org/10.5281/zenodo.7933674>). Model configuration files and post-processing scripts are preserved in GitHub and Zenodo via DOI: <https://doi.org/10.5281/zenodo.7935025> (<https://doi.org/10.5281/zenodo.7935025>).

## References

- Brink, K. (1991). Coastal-trapped waves and wind-driven currents over the continental shelf. *Annual Review of Fluid Mechanics*, 23(1), 389–412. <https://doi.org/10.1146/annurev.fl.23.010191.002133>
- Brink, K. H. (2018). *Stable coastal-trapped waves with stratification, topography and mean flow*. Woods Hole Open Access Server. Retrieved from <https://hdl.handle.net/1912/10527>
- Cerovečki, I., Orlić, M., & Hendershott, M. C. (1997). Adriatic seiche decay and energy loss to the Mediterranean. *Deep Sea Research Part I: Oceanographic Research Papers*, 44(12), 2007–2029. [https://doi.org/10.1016/S0967-0637\(97\)00056-3](https://doi.org/10.1016/S0967-0637(97)00056-3)
- Christensen, J., NielsRené, V., & Gutiérrez, G. V. (1983). A study of sub-inertial waves off the west coast of Mexico. *Deep Sea Research Part A: Oceanographic Research Papers*, 30(8), 835–850. [https://doi.org/10.1016/0198-0149\(83\)90003-1](https://doi.org/10.1016/0198-0149(83)90003-1)
- Connolly, T. P., & Hickey, B. M. (2014). Regional impact of submarine canyons during seasonal upwelling. *Journal of Geophysical Research: Oceans*, 119(2), 953–975. <https://doi.org/10.1002/2013JC009452>

## Acknowledgments

This publication uses results from the CASE project courtesy of Ganesh Gopalakrishnan. BDC, STG, and MRM have been supported by the NASA Surface Water and Ocean Topography Science Team (award 80NSSC20K1136), and STG has also received support from the NASA Ocean Vector Winds Science Team (award 80NSSC19K0059).



- Cushman-Roisin, B., Willmott, A. J., & Biggs, N. R. (2005). Influence of stratification on decaying surface seiche modes. *Continental Shelf Research*, 25(2), 227–242. <https://doi.org/10.1016/j.csr.2004.09.008>
- Dobashi, Y., & Inazu, D. (2021). Improving detectability of seafloor deformation from bottom pressure observations using numerical ocean models. *Frontiers of Earth Science*, 8, 621. <https://doi.org/10.3389/feart.2020.598270>
- Dong, C., Idica, E. Y., & McWilliams, J. C. (2009). Circulation and multiple-scale variability in the Southern California Bight. *Progress in Oceanography*, 82(3), 168–190. <https://doi.org/10.1016/j.pocean.2009.07.005>
- Duhaut, T. H. A., & Straub, D. N. (2006). Wind stress dependence on ocean surface velocity: Implications for mechanical energy input to ocean circulation. *Journal of Physical Oceanography*, 36(2), 202–211. <https://doi.org/10.1175/JPO2842.1>
- Durazo, R. (2015). Seasonality of the transitional region of the California Current System off Baja California. *Journal of Geophysical Research: Oceans*, 120(2), 1173–1196. <https://doi.org/10.1002/2014JC010405>
- Durazo, R., & Baumgartner, T. R. (2002). Evolution of oceanographic conditions off Baja California: 1997–1999. *Progress in Oceanography*, 54(1–4), 7–31. [https://doi.org/10.1016/S0079-6611\(02\)00041-1](https://doi.org/10.1016/S0079-6611(02)00041-1)
- GEBCO, C. G. (2020). GEBCO 2020 grid. <https://doi.org/10.5285/a29c5465-b138-234d-e053-6c86abc040b9>
- Georgi, H. (1993). Forced oscillation and resonance. In *The physics of waves* (pp. 44–48). Prentice Hall.
- Gómez-Valdivia, F., Parés-Sierra, A., & Laura Flores-Morales, A. (2017). Semiannual variability of the California undercurrent along the Southern California Current System: A tropical generated phenomenon. *Journal of Geophysical Research: Oceans*, 122(2), 1574–1589. <https://doi.org/10.1002/2016JC012350>
- Gopalakrishnan, G., & Cornuelle, B. D. (2019). Palau's effects on regional-scale ocean circulation. *Oceanography*, 32(4), 126–135. <https://doi.org/10.2307/26845645>
- Hersbach, H., Bell, B., Berrisford, P., Biavati, G., Horányi, A., Muñoz Sabater, J., et al. (2018). ERA5 hourly data on single levels from 1979 to present. Copernicus climate change Service (C3S) climate data Store (CDS). <https://doi.org/10.24381/cds.adbb2d47>
- Hickey, B. M. (1979). The California Current System—Hypotheses and facts. *Progress in Oceanography*, 8(4), 191–279. [https://doi.org/10.1016/0079-6611\(79\)90002-8](https://doi.org/10.1016/0079-6611(79)90002-8)
- Hickey, B. M. (1998). Coastal oceanography of Western North America from the tip of Baja California to Vancouver Island. In A. R. Robinson, & K. H. Brink (Eds.), *The global coastal ocean: Regional studies and syntheses* (Vol. 11, pp. 345–393). John Wiley and Sons.
- Hickey, B. M., Dobbins, E. L., & Allen, S. E. (2003). Local and remote forcing of currents and temperature in the central Southern California Bight. *Journal of Geophysical Research*, 108(C3), 3081. <https://doi.org/10.1029/2000JC000313>
- Hughes, C. W., Fukumori, I., Griffies, S. M., Huthnance, J. M., Minobe, S., Spence, P., et al. (2019). Sea level and the role of coastal trapped waves in mediating the influence of the open ocean on the coast. *Surveys in Geophysics*, 40(6), 1467–1492. <https://doi.org/10.1007/s10712-019-09535-x>
- Huthnance, J., Mysak, L., & Wang, D.-P. (1986). Coastal trapped waves. In *Baroclinic processes on continental shelves* (pp. 1–18). American Geophysical Union (AGU). <https://doi.org/10.1029/CO003p0001>
- Kämpf, J., & Chapman, P. (2016). The functioning of coastal upwelling systems. In *Upwelling systems of the world: A scientific journey to the most productive marine ecosystems* (pp. 31–65). Springer International Publishing. [https://doi.org/10.1007/978-3-319-42524-5\\_2](https://doi.org/10.1007/978-3-319-42524-5_2)
- Kerry, C. G., Powell, B. S., & Carter, G. S. (2013). Effects of remote generation sites on model estimates of M2 internal tides in the Philippine Sea. *Journal of Physical Oceanography*, 43(1), 187–204. <https://doi.org/10.1175/JPO-D-12-081.1>
- Klymak, J. (2017). The Garrett and Munk internal wave spectra matlab toolbox. Retrieved from <http://jklymak.github.io/GarrettMunkMatlab>
- Large, W. G., & Pond, S. (1981). Open ocean momentum flux measurements in moderate to strong winds. *Journal of Physical Oceanography*, 11(3), 324–336. [https://doi.org/10.1175/1520-0485\(1981\)011<0324:OOMFMI>2.0.CO;2](https://doi.org/10.1175/1520-0485(1981)011<0324:OOMFMI>2.0.CO;2)
- Li, X., Zhang, W. G., & Rong, Z. (2021). The interaction between warm-core rings and submarine canyons and its influence on the onshore transport of offshore waters. *Journal of Geophysical Research: Oceans*, 126(12), e2021JC017989. <https://doi.org/10.1029/2021JC017989>
- Lynn, R. J., & Simpson, J. J. (1987). The California Current System: The seasonal variability of its physical characteristics. *Journal of Geophysical Research*, 92(C12), 12947–12966. <https://doi.org/10.1029/JC092iC12p12947>
- Marshall, J., Adcroft, A., Hill, C., Perelman, L., & Heisey, C. (1997). A finite-volume, incompressible Navier-Stokes model for studies of the ocean on parallel computers. *Journal of Geophysical Research*, 102(C3), 5753–5766. <https://doi.org/10.1029/96JC02776>
- Mazloff, M. R., Cornuelle, B., Gille, S. T., & Wang, J. (2020). The importance of remote forcing for regional modeling of internal waves. *Journal of Geophysical Research: Oceans*, 125(2), e2019JC015623. <https://doi.org/10.1029/2019JC015623>
- Medjdoub, K., Jánosi, I. M., & Vincze, M. (2021). Laboratory experiments on the influence of stratification and a bottom sill on seiche damping. *Ocean Science*, 17(4), 997–1009. <https://doi.org/10.5194/os-17-997-2021>
- Molemaker, M. J., McWilliams, J. C., & Dewar, W. K. (2015). Submesoscale instability and generation of mesoscale anticyclones near a separation of the California Undercurrent. *Journal of Physical Oceanography*, 45(3), 613–629. <https://doi.org/10.1175/JPO-D-13-0225.1>
- Moore, A. M., Arango, H. G., Broquet, G., Edwards, C., Veneziani, M., Powell, B., et al. (2011). The Regional Ocean Modeling System (ROMS) 4-dimensional variational data assimilation systems: Part II—performance and application to the California Current System. *Progress in Oceanography*, 91(1), 50–73. <https://doi.org/10.1016/j.pocean.2011.05.003>
- Nelson, A., Arbic, B., Menemenlis, D., Peltier, W., Alford, M., Grisouard, N., & Klymak, J. (2020). Improved internal wave spectral continuum in a regional ocean model. *Journal of Geophysical Research: Oceans*, 125(5), e2019JC015974. <https://doi.org/10.1029/2019JC015974>
- Neveu, E., Moore, A. M., Edwards, C. A., Fiechter, J., Drake, P., Crawford, W. J., et al. (2016). A historical analysis of the California Current circulation using ROMS 4D-var: System configuration and diagnostics. *Ocean Modelling*, 99, 133–151. <https://doi.org/10.1016/j.ocemod.2015.11.012>
- Orlanski, I. (1976). A simple boundary condition for unbounded hyperbolic flows. *Journal of Computational Physics*, 21(3), 251–269. [https://doi.org/10.1016/0021-9991\(76\)90023-1](https://doi.org/10.1016/0021-9991(76)90023-1)
- Palma, E. D., & Matano, R. P. (1998). On the implementation of passive open boundary conditions for a general circulation model: The barotropic mode. *Journal of Geophysical Research*, 103(C1), 1319–1341. <https://doi.org/10.1029/97JC02721>
- Parsmar, R., & Stigebrandt, A. (1997). Observed damping of barotropic seiches through baroclinic wave drag in the Gullmar Fjord. *Journal of Physical Oceanography*, 27(6), 849–857. [https://doi.org/10.1175/1520-0485\(1997\)027<0849:ODOBST>2.0.CO;2](https://doi.org/10.1175/1520-0485(1997)027<0849:ODOBST>2.0.CO;2)
- Penven, P., Marchesiello, P., Debreu, L., & Lefèvre, J. (2008). Software tools for pre- and post-processing of oceanic regional simulations. *Environmental Modelling & Software*, 23(5), 660–662. <https://doi.org/10.1016/j.envsoft.2007.07.004>
- Rabinovich, A. B. (2010). Seiches and harbor oscillations. In *Handbook of coastal and ocean engineering* (pp. 193–236). World Scientific.
- Saldías, G. S., Ramos-Musale, K., & Allen, S. E. (2021). Circulation and upwelling induced by coastal trapped waves over a submarine canyon in an idealized eastern boundary margin. *Geophysical Research Letters*, 48(11), e2021GL093548. <https://doi.org/10.1029/2021GL093548>
- Siyabolola, O. Q., Buijsman, M. C., Delpech, A., Renault, L., Barkan, R., Shriver, J. F., et al. (2023). Remote internal wave forcing of regional ocean simulations near the US West Coast. *Ocean Modelling*, 181, 102154. <https://doi.org/10.1016/j.ocemod.2022.102154>

- Todd, R. E., Rudnick, D. L., Mazloff, M. R., Davis, R. E., & Cornuelle, B. D. (2011). Poleward flows in the southern California Current System: Glider observations and numerical simulation. *Journal of Geophysical Research*, *116*(C2), C02026. <https://doi.org/10.1029/2010JC006536>
- Vallis, G. K. (2017). *Atmospheric and oceanic fluid dynamics*. Cambridge University Press.
- Vazquez, H. J., & Gomez-Valdes, J. (2021). Wind events in a subtropical coastal upwelling region as detected by admittance analysis. *Ocean Dynamics*, *71*(5), 493–507. <https://doi.org/10.1007/s10236-021-01446-z>
- Verdy, A., Mazloff, M. R., Cornuelle, B. D., & Kim, S. Y. (2014). Wind-driven sea level variability on the California coast: An adjoint sensitivity analysis. *Journal of Physical Oceanography*, *44*(1), 297–318. <https://doi.org/10.1175/JPO-D-13-018.1>
- Watts, D. R., Wei, M., Tracey, K. L., Donohue, K. A., & He, B. (2021). Seafloor geodetic pressure measurements to detect shallow slow slip events: Methods to remove contributions from ocean water. *Journal of Geophysical Research: Solid Earth*, *126*(4). <https://doi.org/10.1029/2020JB020065>
- Xu, Y., Watts, D. R., Wimbush, M., & Park, J.-H. (2007). Fundamental-mode basin oscillations in the Japan/East Sea. *Geophysical Research Letters*, *34*(4), L04605. <https://doi.org/10.1029/2006GL028755>